The University of Queensland

Bachelor of Engineering Thesis

Investigating Mode I and Mixed Mode Fracture Toughness Values in Fibre Metal Laminates

Student Name (#): Shane Evans

Course Code: MECH4501

Supervisor: Martin Veidt

Submission Date: 1 June 2018

A Thesis Report submitted in partial fulfilment of the requirements of the Bachelor of Engineering Degree in Mechanical Engineering

UQ Engineering

Faculty of Engineering, Architecture and Information Technology

Abstract

The military, bio-medical and particularly aerospace industries are continually motivated to produce materials which inhibit increased mechanical properties. This has led to advanced material design stemming from combining materials in hopes of producing a more established hybrid material which exceeds the limitations of each individual material constituent. Over the past 70 years and substantially over the last twenty years, this has led to the development of Fibre Metal Laminates (FMLs) which consist of thin layered composite/metal alloy sheets. Particularly, FMLs offer; increased impact tolerances, fatigue resistance and a higher modulus of elasticity albeit at lower densities.

FMLs and their implementation into the commercial industry however has been delayed due to their susceptibility to fail prematurely at the interface thus leading to their strict manufacturing procedures. Furthermore, assessing the failure at the FML interface is difficult and requires advanced measurement techniques and experimental testing procedures. A newly developed measurement technique labelled the Top Surface Analysis (TSA) provides the means to overcome this issue by taking significant efforts to capture information leading to improved fracture property estimates.

This Thesis project presents a method towards a manufacturing procedure and a experimental test technique in order to estimate the mode I and mixed mode fracture properties of an FML material made up of Glass Fibre Reinforced Polymer (GFRP) and steel. Furthermore, it outlines the methodology undertaken to correlate results between the newly developed TSA technique in comparison to the conventional side view method using two reduction schemes; the Modified Beam Theory (MBT) and J-integral. Providing a further comparison to the measurement technique estimates, a Finite Element Methods (FEM) labelled the Virtual Crack Closure Technique (VCCT) is developed which provides simplicity in confirming mode I and mixed mode values.

The mode I samples have been experimentally tested using the Double Cantilever Beam (DCB) procedure. Upon testing, the results indicated that one of the two samples have had their interfaces compromised due to non-ideal bonding between the GFRP and steel substrates. However, one of the samples still exhibited a saw-tooth response typical in FMLs. Furthermore, voids along the edge of the samples were identified impacting the side view measurement technique by prematurely approximating the crack length. In addition, instability issues prevented the TSA technique in providing any estimates. The side view measurement technique however was capable of capturing both ideal and non-ideal delamination with the MBT and J-integral schemes successfully identifying between stable and unstable crack growth, albeit at various fracture values.

The mixed mode samples were tested using a modification of the DCB test, labelled the Asymmetric Double Cantilever Beam (ADCB) procedure. The results provided that ideal bonding has occurred between the two samples tested by observing a typical FML load-displacement response. Furthermore, the load-displacement response differed to that observed in mode I indicating the influence of mode II. Observed across one of the samples, premature failure is observed brought on by the onset of corrosion on the steel's surface. Both the TSA and side view measurement techniques indicated consistency in identifying similar trends across the two samples tested thus indicating their success. TSA indicated its ability to capture the fracture properties across the width of the samples, a feat the conventional side view method is unable to achieve. The TSA measurement technique further indicated its success in conjunction with the MBT method providing results in close proximity to the VCCT model presented as well as the ability to identify the crack initiation earlier which led to lower overall fracture property estimates.

Due to the mode I's TSA instabilities and voids along the samples edges, there exists large uncertainties with the results restricting the ability to provide a quantifiable comparison. However, it is reasoned upon further testing that fracture values using the side view measurement technique in conjunction with MBT will be able to be distinguished between mode I and mixed mode samples. Furthermore, both the TSA and side view measurement techniques using the J-integral indicate a strong correlation to identify between mode I and mixed mode loading.

Overall, the project experienced first hand the liability of non-ideal bonding between the FML interface resulting in premature delamination thus providing considerably lower fracture properties. The TSA measurement technique although requiring additional calibration and setting up, provides increased efforts to approximate the crack length leading to defined fracture properties. Furthermore, the side view and TSA measurement techniques in conjunction with the J-integral provides a promising tool to assess future FMLs.

Acknowledgements

First and foremost, I would like to thank my advisor throughout this Thesis topic, A/Prof. Martin Veidt for his endless guidance, support and encouragement. You have provided me with the resources and knowledge to make this Thesis possible and I appreciate you giving me the opportunity to experience hybrid composite structures.

In addition, I would like to also thank Kurt Mills for his time in manufacturing the hybrid samples. Furthermore, for his abilities in calibrating the measurement techniques and microscopy images.

Finally, I would like to thank all other members that made the time to discuss ideas and provide clarity to tasks and results. These people include; Dr. Juan P. Torres who demonstrated the measurement techniques, Mitch Dunn who arranged the composite samples being water-jet cut and Dr. Michael Heitzmann who provided the FEM knowledge.

Contents

List of Tables

List of Figures

Nomenclature

$-dU_p$	Reduction of Stored Potential Energy in the System
Δ	MBT Correction Factor / Difference in Observed Values
δ	Deflection of the Sample
σ	Far-Field Stress
a	Crack Length upon Delamination
a_o	Initial Crack Length
B	Sample Width
C	Compliance of a Material / Line Integral Surrounding the Crack tip
d	Displacement of Sample (INSTRON Output)
d^*	Crack Tip Opening Displacement
d_y	Displacement Input of FEM Model
d_z	Displacement of Individual TSA Points (ARAMIS Output)
$d_z^{central}$	Central Axis Displacement
d_z^{local}	Local Displacement
dA	Per Unit Crack Area Created
E	Young's Modulus
G / J	Strain Energy Release Rate
G_c	Critical Strain Energy Release Rate
G_T	Total Strain Energy Release Rate
h	Samples Height
I	Samples Inertia
$J_{I\infty}$ / $G_{I\infty}$	Steady State Strain Energy Release Rate of Mode I
J_{Ic} / G_{Ic}	Critical Strain Energy Release Rate of Mode I

K	Stress Intensity Factor
k	Parameter Accounting for Symmetric / Asymmetric Load Cases
K_c	Critical Stress Intensity Factor
L	Sample Length
P	Force (Load)
R	Reaction Forces
u	Displacement corresponding to x
v	Displacement corresponding to y
Y	Geometric Factor
ADCB	Asymmetric Double Cantilever Beam
ANSYS	ANlysis of SYStems
APDL	ANSYS Parametric Design Language
ARALL	ARamid ALuminium Laminates
ARAMIS	Software used in conjunction with the TSA technique
ASTM	American Society for Testing and Materials
CARALL	CArbon Reinforced ALluminium Laminates
CTOD	Crack Tip Opening Displacement
CZM	Cohesive Zone Method
DCB	Double Cantilever Beam
DIC	Digital Image Correlation
EPFM	Elastic Plastic Fracture Mechanics
FEM	Finite Element Methods
FML	Fiber Metal Laminates
GFRP	Glass Fibre Reinforced Polymer
GLARE	GLass Laminate Aluminium Reinforced Epoxy
INSTRON	Testing Equipment (Machinery)
LEFM	Linear Elastic Fracture Mechanics
SERR	Strain Energy Release Rates
SIF	Stress Intensity Factor
TSA	Top Surface Analysis
UQ	The University of Queensland
VCCT	Virtual Crack Closure Technique

Chapter 1

Introduction

With the continual push for more light weight, robust and increased mechanical properties, material development continues to be at the forefront of engineering design. This has led to the development of GLARE (GLass Laminate Aluminium Reinforced Epoxy), a material being made up of thin aluminium layers bonded together with glass fibres arriving after two decades of experimental testing and analysis techniques [50, 58]. The major advantage of these hybrid composites, or Fibre Metal Laminates (FMLs) as they are now known is in their ability to strongly influence the mechanical properties by altering the layup of the fibres, stacking sequence, or combination of materials as well as varying the thickness of the metal alloy. This variety makes them susceptible to fill a wide range of engineering applications with FMLs being used extensively due to their high fracture and impact resistant properties [63]. However, due to their arrangement of containing multiple materials and additional manufacturing requirements, it becomes substantially more complex to measure accurate fracture values along their interfaces. It is well documented that FML interfaces are susceptible to premature failure by adhesive debonding due to stress concentrators and voids on the free edges [45]. This raises issues for the requirement of reliable experimental procedures, measuring techniques as well as Finite Element Methods (FEM) in order to obtain accurate fracture properties.

One recently developed optical technique that is gaining interest is the Top Surface Analysis (TSA) technique due to its ability to supersede complications in the conventional side view [45]. TSA is the method of analysing the top surface of a specimen utilised in conjunction with Digital Image Correlation (DIC), the technique that processes strain and deformation information. Therefore, a Fibre Metal Laminate made up of Glass Fibre Reinforced Polymer (GFRP) and steel is investigated further through the TSA and side view measurement techniques as well as FEM models to assess the fracture properties at the interface by carrying out a Double Cantilever Beam and Asymmetric Double Cantilever Beam (DCB & ADCB) test procedures.

1.1 Problem and Motivation

FMLs inhibit advantageous mechanical properties in comparison with their individual material constituents. However, since their early development, their progress to be implemented into commercial industries has been halted due to their susceptibility to prematurely delaminate along the interface. Therefore, development is required in determining a method suitable to manufacture and analyse the FML interface such that they newly developed FMLs may be more rapidly introduced into industries of interest.

Assessing the failure at interfaces is difficult however and requires experimental procedures and measurement techniques to accurately determine their fracture properties. The purpose of this Thesis is therefore to determine the fracture properties at the FML interface using the newly developed Top Surface Analysis technique in comparison with the conventional side view, which contains its own areas of concern due to relying on the skillset of the user in approximating delamination.

Therefore, TSA and side view measurement techniques will be carried out and compared with FEM results on two sets of samples. Initially, a mode I test was will be carried out before experimenting on a mixed mode test case. This is to conclude possible limitations in the TSA and side view measurement techniques, identify areas of further development as well as conclude on if the test procedure carried out is able to distinguish between mode I and mixed mode fracture. This will allow further development to the progress of FMLs, quantify the fracture properties of the GFRP-steel FML investigated as well as provide The University of Queensland (UQ) with a new measurement technique for further FMLs of interest.

1.2 Scope / Objectives

The scope is indicated in Table 1.1 with the project to be completed by June 2018.

Table 1.1: Project scope

In Scope	Out of Scope
Mode I / mixed mode test configurations	Mode II / Mode III test configurations
Side view analysis	Failure modes
Fibre Metal Laminates	Fatigue failure
FEM methods	Dynamic loading processes
Fabrication and surface treatment of FMLs	Tensile testing
TSA analysis	Hardness testing

Overall, the objectives of the project include:

1. To produce a manufacturing procedure for FMLs and a measurement technique method to specify mixed the fracture properties.

    - This method will have the ability successfully manufacture FML materials as well as distinguish between mode I and mixed mode fracture properties. FEM analysis and TSA literature is to provide the results and information necessary to provide clarity to the task.

2. Correlate data between FEM results as well as the TSA and side view measuring techniques for mode I and mixed mode fracture properties.

    - To experimentally test TSA and side view measurement techniques in a mode I and mixed mode test procedures. The mode I is to provide the basis of results for the FMLs with the mixed mode to quantify the influence of mode II properties. FEM will further provide results and allow a direction comparison between theoretical and experimental values.

1.3 Methodology

The following methodology has been applied as part of the project:

1. Project planning.
    - Resource Management, including a Gantt Chart and Risk Assessment has been developed initially in the first semester (see Appendix A.1) such that it may provide adequate time for each necessary stage as well as indicate milestones to manage the project effectively. The scope of the project must also be well defined in order to satisfy The University of Queensland (UQ) requirements.
2. Literature review.
    - Past studies and projects are to indicate gaps of knowledge. Additionally, this will provide the information and reasoning behind the majority of chosen processes, these include; testing procedures, fracture mechanics, FML manufacturing and their interests in the industry, FEM methods/analysis and TSA and side view measurement techniques.
3. Material manufacturing.
    - Providing the steps and tasks undertaken as well as identifying any areas of concern or potential risks before the testing of the specimens.
4. TSA and side view setup
    - Outlining the methodology carried out using the TSA and side view measurement techniques.
5. Testing of specimens.
    - Execution of experimental testing in conjunction with TSA and side view.
6. Results / Discussion / Conclusion.
    - Compare the TSA and side view results in comparison with FEM and determine whether the measurement techniques are able to identify between mode I and mixed mode samples. Furthermore, to conclude on the results and suggest areas for further improvement as well as the requirements for next stage development.

1.4 Expected Outcomes / Goal

It is expected that the TSA and measurement techniques are capable of quantifying the fracture properties between mode I and mixed mode samples. Therefore, this is to provide the UQ Composites faculty with a powerful measurement technique to determine fracture toughness properties of FMLs.

Additionally, that FEM is successful in capturing mode I and mixed mode fracture properties. This has the major benefit of being able to approximate fracture characteristics before testing commences as well as confirm if mixed mode loading occurs.

Chapter 2

Literature Review

In order to obtain the expected outcomes, research is required across a variety of topics. These include; **Fracture Mechanics** - containing a brief overview to crack propagation, failure mode theory and information on Strain Energy Release Rates, **Top Surface & Side View Measurement Techniques** - an introduction to the requirements, procedures and method of implementation in order to obtain results, **Experimental Test Procedures** - including the methods to test the fracture properties of the FML as well as determine whether TSA is compatible (not restricting the top surface), **Fibre Metal Laminates** - citing the reason for the FML chosen and their interests in real world scenarios and **FEM** - the selection of computer software to provide results, the approach taken to calculate fracture properties in mode I and mixed mode samples as well as outline the procedure to obtain results for comparison.

2.1 Fracture Mechanics

Fracture mechanics relates to the study of crack propagation through materials and how materials experience failure. Two major approaches exist in studying crack propogation which define the Stress Intensity Factor (SIF) or more simply, the fracture toughness, denoted 'K' and the Strain Energy Release Rates (SERR), denoted 'G' [7]. The two approaches include:

1. **Linear Elastic Fracture Mechanics (LEFM)** - Based on Griffith's Equation (Equation 2.1) which assesses the severity of the stress field around the crack and is calculated by the far-field stress (σ), a geometric factor (Y) and initial crack length (a). It assumes linear deformation is confined to a region surrounding the crack.

2. **Elastic Plastic Fracture Mechanics (EPFM)** - Applied to materials exhibiting non-linear deformation and assesses an independent line integral surrounding the crack tip.

$$K = Y\sigma\sqrt{\pi a} \tag{2.1}$$

Strain Energy Release Rates

SERR (G) values is described in Equation 2.2. It is calculated by the reduction of stored potential energy in the system ($-dU_p$) with respect to per unit crack area created (dA), or rather, the amount of energy to break the atomic structure of the material. Additionally,

in order for a crack to propagate it is the requirement that the experienced SERR values (G) exceeds the critical SERR (G_c). It is also expressed in SIFs as stated in Equation 2.3.

$$G = \frac{-dU_p}{dA} \tag{2.2}$$

$$\begin{cases} G > G_c \\ K > K_c \end{cases} \tag{2.3}$$

Knowing the critical values is of great important to newly developed materials as it is these intrinsic properties that conclude whether a specimen will fracture. In addition, it also raises the importance of being capable of implementing test procedures to isolate and determine the accuracy in these critical values.

2.1.1 Mixed Mode Energy Release Rates

The fracture of materials may occur by a combination of three modes. Figure 2.1 displays the modes experienced on a specimen which includes; Mode I - Opening shear, Mode II - In-plane shear and Mode III - Out-of-plane shear. For simplicity, each mode corresponds to its specific subscript denoted by G_I, G_{II} and G_{III}. Overall, the total SERR value is simply the sum of each experienced mode; $G_T = G_I + G_{II} + G_{III}$ with the critical SERR modal values stated by the nomenclature; G_{Ic} etc.

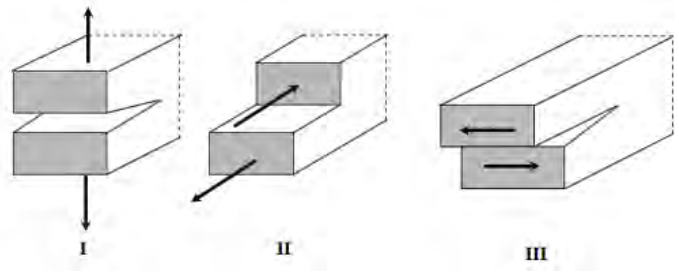

Figure 2.1: Modes of fracture [27]

Depending on the geometric loadings a specimen experiences, it is possible to isolate one or a combination of these modes. The purpose of identifying the three modes is to allow a specimen to undergo mode I and mixed mode loading where mixed mode for this project is quantified by mode I and mode II only ($G_{III} = 0$).

An orthotropic material experiencing only mode I SERR values will be dependent on a symmetric specimen across its thickness as provided in 2.1. For mixed mode, an asymmetric mode I loading configuration will create a mixture of mode I and mode II SERR values. Therefore, for the case of an orthotropic material, such as a Fibre Metal Laminate sample, further calculations are required to ensure only mode I occurs as later indicated (refer Section 2.4).

2.2 Top Surface & Side View Measurement Techniques

2.2.1 Top Surface Analysis

TSA is the technique which analyses the top surface of a specimen. However, in order to capture information the TSA technique requires Digital Image Correlation (DIC), explained as the method that captures the information (cameras etc.) and ARAMIS, the software the processes the information. It is the purpose of analysing the top surface as it has the ability to bypass the conventional side view technique by indicating the crack length across the materials width. Throughout testing, ARAMIS extracts relevant strain and deformation data with Figure 2.2 indicating TSAs components.

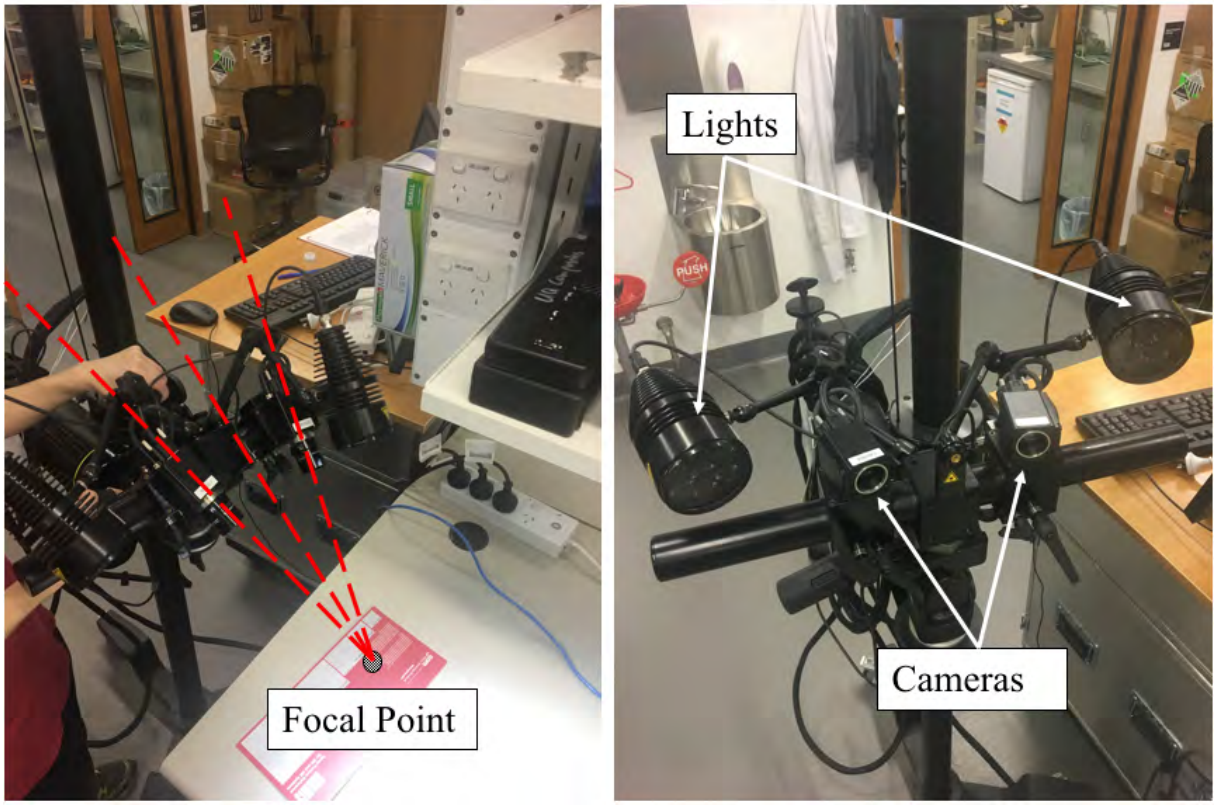

Figure 2.2: TSA apparatus

It is arranged such that two cameras are positioned by a magnitude length (3D coordinate system) and angular direction (symmetric around the focal point), both of which are pre-determined by the ARAMIS manual by knowing the specimen test size and speckle pattern. It is the arrangement of the speckle pattern that allows the TSA technique to collect the relative displacement of each individual point. In doing so, contour plots of strain and deformation data are produced with the largest magnitude values (difference in displacement) indicating the most and least compliant sections, thus approximating a crack length. This is more easily visualised in Figure 2.5.

Reiner et al. [45] concluded TSAs effectiveness in the development of mode I fracture properties. In addition, it was stated that in comparison to the conventional side view analysis, estimates were slightly lower (however both were successful) in Glass Fibre Reinforced Polymer (GFRP) samples at crack propagation. This is explained due to the side views tendency to prematurely approximate the crack length due to fracture initiating on the edges of the material. Chu et al. [21] provided the benefits of DIC with experiments

on aluminium specimens and revealed the importance of optimising image resolution. In addition, laser speckle patterns raised issues with decorrelation at small strains as a result of poor image quality. Yoneyama et al. [64] expressed DICs simplicity in calculating mixed mode SIFs in PolyMehtylMethAcrylate (PMMA) specimens with a relative degree of success.

Furthermore, various authors have raised concerns specifically for DIC analysis including adhesive debonding due to displacement discontinuities [17, 45] as well as its limitation in interlaminar toughened aerospace epoxy formulations under mixed mode loading (loss of reference points to measure the crack length) [34].

2.2.2 Side View Analysis

The conventional side measurement technique focuses on the side of the sample in order to approximate the crack length. This is presented in Figure 2.3. The major limitation with side view measurements is its lack of ability to determine where crack initiation first begins and is for this reason why TSA has been developed, in attempts to supersede the conventional method [43].

Figure 2.3: DCB side view measurement technique

2.3 Experimental Test Procedures

Experimental tests are required in order to support and validate the FEM method as well as compare the TSA and side view measurement techniques. Currently, there exists recognised test procedures for assessing the fracture toughness of materials by the American Society for Testing and Materials (ASTM) [1].

2.3.1 Mode I

To determine mode I SERR values, the DCB test provided by ASTM D5528 [23] will be carried out as it is an internationally recognised test procedure. It describes the experimental procedures as well as data reduction schemes in order to approximate critical mode I SERR values (G_{Ic}). Figure 2.4 provides the DCB test schematic requirements indicating the samples geometric layout including; height 'h', width 'B', length 'L' and pre-crack (labelled insert) 'a_o'. The pre-crack is required in order to define where delamination occurs and is created by inserting a pre-film between the FML interface.

The DCB test requires loading blocks in order to test the sample. The test equipment chosen to conduct the DCB test procedure is the INSTRON tensile test machine which

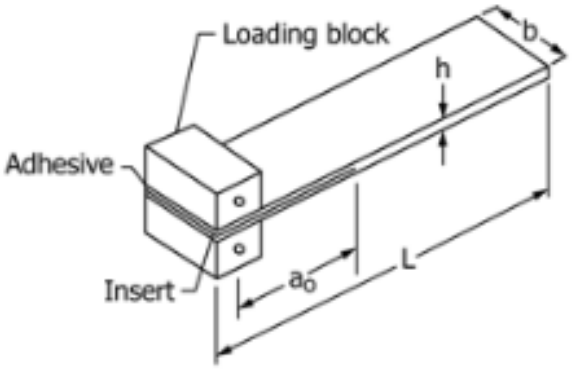

Figure 2.4: DCB test schematic [23]

has the ability to load the sample at a controlled displacement rate. Furthermore, in order to comply with ASTM D5528 standards, guidelines are specified. These include:

- Minimum geometric constraints consisting of; L = 125mm, B = 25mm, $a_o = 47.5$mm;
- Displacement controlled loading within the rage of; 0.5 - 5 mm/min;
- To implement the data reduction scheme labelled the Modified Beam Theory as it yields the most conservative results; and
- At least five samples in order to obtain accurate fracture values.

2.3.2 Mixed Mode

Various test procedures exist in order to isolate specific fracture properties however, various authors debate over the most reliable test procedure to calculate mixed mode loading. This therefore requires research in order to determine a suitable test procedure that allows TSA and side view measurement techniques to measure the crack length.

Mixed mode test procedures have been developed with the Mixed Mode Bending (MMB) procedure provided by ASTM D6671 [24] and the Asymmetric Double Cantilever Beam (the same as the DCB test procedure however with varying thickness') tests being the most widely recognised in determining SERR values [25]. Therefore, these two test procedures are further investigated to determine which is more suitable for the FML.

Numerous authors have conflicting approaches in calculating mixed mode SERR values. For the Asymmetric Double Cantilever Beam (ADCB) test, Williams [61] concluded the test procedure predicted mode I for any asymmetric ratio with results diverging from 34% to 1% error in composite structures. Charalambides et al. [20] concluded precision in mixed mode stating within 8% to theoretical calculations. This however was stated under the circumstance that mode I was dominant in the ADCB tests. Molln et al. [39] further provided results that agree well for ADCB mixed mode test procedure with values providing 5% error.

In comparison, Ducept et al. [25] indicated the MMB tests favourability however concluded that both test procedures were adequate in calculating mixed mode SERR values. Bennati and Valvo [13] further concluded preference in regard to the MMB test procedure.

An ADCB test procedure is selected from assessing various author recommendations, its ability to not restrict the top surface when being displaced as well being able to be

carried out following the DCB test procedure provided in mode I. Therefore, mode I's ASTM D5528 guidelines is adapted to for the mixed mode loading case. This is to ensure a quantifiable comparison between the mode I properties for mode I and mixed mode samples. An ADCB test schematic is provided in Figure 2.7 for clarity.

DCB & ADCB Test Experiments Using Top Surface Analysis

TSA has previously been successful for mode I values from Reiner [43, 45]. It is from the findings and information provided here that is to be adapted to the ADCB test procedures. Figure 2.5 in conjunction with the following describes the TSA technique explanation in reference to the DCB and ADCB test procedure.

The top surface contour lines refer to the vertical displacement of the sample with respect to the initial starting position. Each surface white line is constructed in order to approximate the current crack length with respect to the samples width and length. By measuring the relative vertical displacements to a reference position, the most and least compliant sections are approximated, thus providing the crack length and location.

The CTOD labelled 'd^*' is evaluated by knowing the relative vertical displacement between each derived surface line, labelled 'd_z^{local}' and the central axis (crack path) '$d_z^{central}$' stated in Equation 2.4.

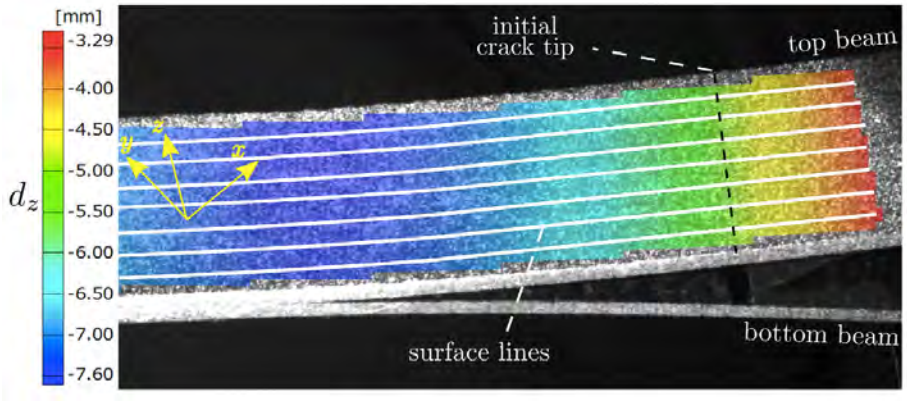

Figure 2.5: Top Surface Analysis displacement processing [45]

It is the purpose of calculating the CTOD in order to approximate a crack length at any given force and displacement. Furthermore, it is from the displacement, crack length and force which allows SERR values to be calculated as later provided in Chapter 5.

$$kd^* = d_z^{local} - d_z^{central} \tag{2.4}$$

The parameter 'k' takes into account asymmetric or symmetric load cases and is calculated by simple beam theory (see Equation 2.5). Note that subscripts 't' and 'b' refer to the top and bottom substrates of the sample.

$$k = \frac{h_b^3 E_b^3}{h_t^3 E_t^3 + h_b^3 E_b^3} \tag{2.5}$$

2.4 Fibre Metal Laminates

FMLs are hybrid laminates consisting of layered sheets of metal alloy and fibre/epoxy composites structures [57]. Due to their hybrid nature, their behaviour is a mixture between

each included material constituent resulting in advantageous properties. Furthermore, they allow variation in their mechanical properties by altering the; metal alloy/composite stacking sequence, the fibre layup direction as well as the overall thickness of each substrate. It is from their continuous advantages that they continue to be of interest as they offer superior mechanical properties in regards to fatigue resistance, damage tolerance, strength and a high modulus of elasticity at low densities.

FMLs have received exponential development over the past decades originating from the Fokker facilities in 1945 [57]. It is from the extensive research over the past 70 years that has allowed FMLs to be developed. The three first developed FMLs continue to be used extensively across the aerospace market with GLass Laminate Aluminium Reinforced Epoxy (GLARE) being selected for the A380 upper fuselage and Boeing 777 [48, 63], Aramid Reinforced ALluminium Laminates (ARALL) which continues to be utilised in supersonic aircraft wings and tails [59] and CArbon Reinforced ALluminium Laminates (CARALL) in aircraft carrier cargo doors [56]. Furthermore, additional hybrid laminate structures have been further implemented over the past two decades with a Carbon Fibre Reinforced Polymer (GFRP)-titanium FMLs being used to improve gas barrier properties in propellent tank applications [40] and graphite-titanium FMLs in the biomedical industry [16].

However, with their ability to supersede conventional materials properties, FMLs require extensive amounts of testing due being susceptible to failures at the interface as well as inhibiting the failures of each respective material included. ARALL, the first developed FML required two decades of research due to premature adhesive debonding between the FML interface brought on by the onset of stress concentrators, voids within the interface and non-ideal bonding between the layers [44, 59]. Debonding is therefore the major concern as it significantly reduces the fracture properties, resulting in inconsistent calculated SERR values.

2.4.1 GFRP-Steel Fibre Metal Laminates

The FML investigated for the project is a Glass Fibre Reinforced Polymer (GFRP) composite structure bonded with a steel laminate as indicated in Figure 2.6. GFRP and steel are extensively used throughout the industrial, energy and marine industries [53, 54]. It is therefore the advantage of combining both the GFRP and steel in order to create a new hybrid composite capable of overcoming the limitations of each material constituent.

Glass Fibre Reinforced Polymers

Glass Fibre Reinforced Polymers is a composite structure made up of a fibre/epoxy matrix. The glass fibres provide the reinforcement to the structure with the epoxy-resin (polymer) referring to the 'glue' which contains the fibres. In regard to glass fibres three main types exist, these include [15, 29]:

1. E-glass fibres: The most common type of fibre making up 90% of the market. It is generally used due to its performance to cost ratio.

2. S or R-glass fibres: Standing for Structure and Reinforcement respectively. They refer to increased mechanical properties to that of E-glass fibres however come at increased costs.

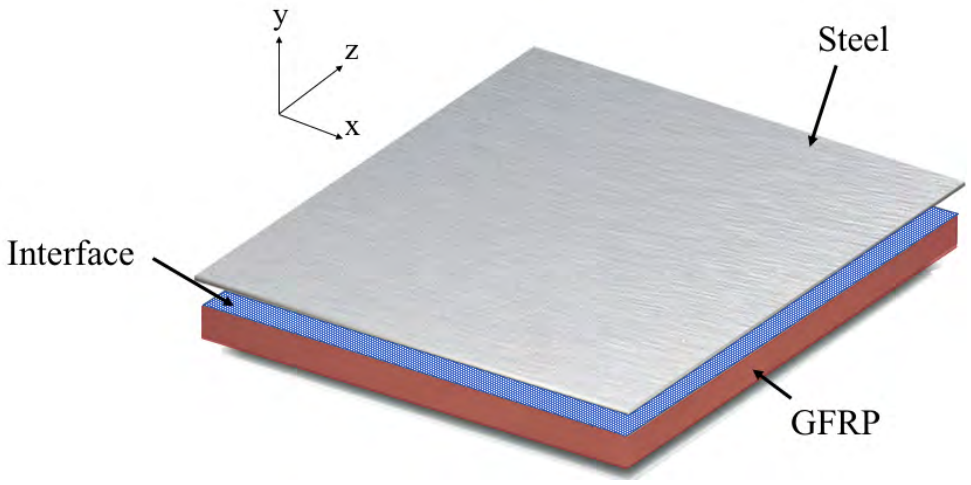

Figure 2.6: GFRP-steel FML

3. D-glass fibres: Fibres inhibiting electrical properties that are extensively used across circuit boards.

In addition, the fibres may be woven together to meet specific mechanical properties. These include; plain, twill, basket, leno and satin methods. In weaving the fibres, sheets are able to be constructed. Furthermore, the sheets are then able to contain pre-impregnated (prepreg) resin systems providing ease in manufacturing. The major advantage of composites is in their ability to alter the fibre direction within each sheet, varying the mechanical properties.

GFRP is utilised across a wide range of engineering disciplines. Since its development in the early 1900's, it has continued to be implemented across the aerospace, marine and energy markets due to its lightweight and high strength charachteristics [55]. In the aerospace market, it has been incorporated due to its excellent strength-to-weight properties and partly makes up 53% of overall composites used in Airbus A350 XWB [38]. Additionally, with the rapid increase of renewable energy, GFRP is used extensively in the production of wind turbines as it offers competitive prices in comparison with Carbon Fibre Reinforced Polymers (CFRP) [62].

GFRP however has limitations such as; low fracture toughness values, the influence of moisture degradation and the delamination upon mechanical impacts as they are prone to fracture in high stress applications [8, 12]. It is from recognising the limitations in GFRP that has led to its development of being bonded with metal alloys.

Steel

Steel has continued to be a material favourite across the machinery, civil, automative and marine industries due to its ability to alloyed with other elements further improving its physical and chemical properties as well as being able to be recycled indefinitely with no loss of mechanical properties [51]. Furthermore, from its developed manufacturing procedures, steel continues to provide the world with 1,800 mega tonnes being consumed in the year 2016 [52].

Steel refers to the alloy of iron within a carbon content range from 0.03 to 1.075%. Steel is of interest to be used with GFRP due to its ability to absorb energy upon im-

pact, thus protecting the GFRP structure, maintaining a high strength and modulus of elasticity.

2.4.2 GFRP-Steel FML Material Properties

The GFRP to be manufactured is made from HexPly 914 S-glass fibre reinforced (twill weave) prepreg sheets 300mm x 300mm [31]. The GFRP material properties are provided in Table 2.1. Due to the GFRPs orthotropic nature, additional material properties are defined with respect to loading direction. This is defined in Figure 2.6 with coordinates (x, y, z) equalling to (11, 22, 33). Nomenclature values that are indicated '12' etc. describe the stresses acting along each face. Table 2.2 indicates the steel and its values. The steel has been chosen to be ASTM-A366 due to its availability, crack resistance properties and material consistency [49].

Table 2.1: HexPly 914 S-glass (twill weave) prepreg properties [31]

Nomenclature	Value
$E_{11} = E_{22}$	19.0 GPa
E_{33}	11.5 GPa
G_{12}	3.45 GPa
$G_{13} = G_{23}$	4.12 GPa
ν_{12}	0.27
$\nu_{13} = \nu_{23}$	0.4
t	0.104mm

Table 2.2: A366 steel material properties [49]

Nomenclature	Value
E_{steel}	200 GPa
ν_{steel}	0.27
t	1.0 & 8.0 mm

Manufacturing & Material Treatment Quality Assurance

It is important to emphasise the phenomenon associated with the composite manufacturing of the FML such as the force-shear stress coupling effects described as the coefficient of mutual influence. This value explains that when loading a composite structure, the normal force, if not applied parallel to the fibre direction, or if the fibre alignment is not parallel with respect to each sheet lay-up, shear stress will propagate through the thickness of the sample further comprimising the FML interface. Furthermore, the requirement of symmetric lay-ups to eliminate coupling between normal and bending reaction forces as described by composite lamina theory [5].

In order for the composite and steel substrate to be successfully bonded, it is critical to prepare the surfaces correctly. Therefore, a strict procedure must be met in order to assert that an ideal bonding scenario has occurred. Table 2.3 provides the mode I and mixed mode samples used for the testing. A total of five specimens is recommended for

each set of samples as specified in the ASTM D5528 [23].

As the GFRP and steel are defined by their own independent material properties. Calculations are required before manufacturing in order to ensure that mode I loading is occurring. Failing to do so would result in the substrates undergoing different deflections when being pulled apart (differ in compliance) further providing no basis of results in comparison to the mixed mode samples. In order to ensure a mode I loading, a 1mm steel substrate is selected and assessed on the thickness required of GFRP to ensure the deflection is equal. This method is provided by beam theory, stated in Equation 2.6 and visually in Figure 2.7 which shows the FML undergoing the ADCB test procedure.

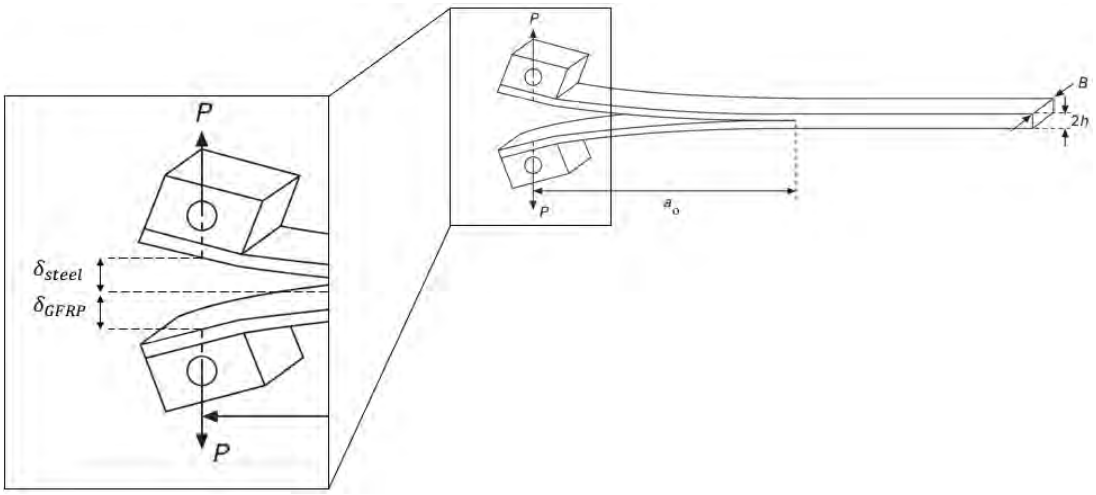

Figure 2.7: Deflection of each FML substrate, adapted from Laffan et al. [35]

$$\delta = \frac{PL^3}{EI} \tag{2.6}$$

Where:
$I = \frac{Bh^3}{12}$

Therefore, by assuming the deflection 'δ' experienced in each substrate is equal. The following relationship allows to assess a mode I case scenario by knowing:

- 'P' equals to the applied load;
- 'E' referring to each materials Young's Modulus;
- 'L, B, h' specifying each substrates length, width and height; and
- 'I' being each substrates inertia.

This method, restricted by the GFRP thickness and properties, calculates deflection values within 3% between each substrate. The to be tested mode I and mixed mode samples and their corresponding thickness' are provided in Table 2.3.

$$h_{GFRP} = \left(\frac{E_{Steel}}{E_{GFRP}}\right)^{\frac{1}{3}} \cdot h_{Steel} \tag{2.7}$$

Investigations from authors state that the anticlastic curvatures of specimens in beam loadings are less significant in thin samples. This is stated as the curvature of a material

Table 2.3: GFRP-steel FML testing samples

Mode Experienced	Steel Thickness (mm)	GFRP Thickness (mm)
Mode I	1.0	2.184 (21 plies)
Mixed Mode	8.0	2.496 (24 plies)

across its width provided in Figure 2.8. This creates additional stress and non-uniform loadings across the material further indicating areas of concern in the mixed mode GFRP-steel sample due to the thickness [43, 44].

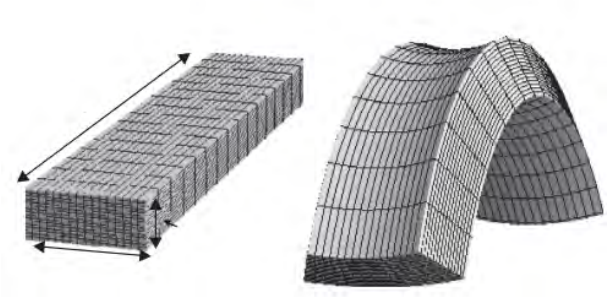

Figure 2.8: Anticlastic curvature [60]

2.5 Finite Element Methods

Finite Element Methods refer to numerical techniques that approximate solutions given initial boundary problem values such as displacements or forces. They provide preliminary solutions to experiments and therefore is a popular method in validating models and obtaining information. FEMs purpose is to justify that the FML samples exhibit mode I and mixed mode SERR values. Two major methods exist in determining SERR values and simulating crack propagation [9, 10, 17, 46]:

- **The Cohesive Zone Method** (CZM) - The method of analysing the interface of where two materials are bonded. The interface is then assessed by analysing the separation distances and stresses allowing crack initiation to be predicted.
- **Virtual Crack Closure Technique** (VCCT) - The approach of analysing the reaction forces and displacements at the crack tip as explained in Figure 2.9. It assumes that the energy required to separate the interface equals the energy required to close it.

For the case of assessing mixed mode failure properties however, only VCCT is capable of this feat and as a result is used in providing SERR values [45].

2.5.1 Virtual Crack Closure Technique

VCCT is capable of producing mixed mode values and is valid for isotropic and anisotropic materials [28]. SERR values are calculated (see Equation 2.8) by evaluating the relative displacements (u, v) and reaction forces (R) of individual nodes (depicted as black dots in Figure 2.9) located at the crack tip.

Qian and Xie [41] successfully modelled isotropic materials through VCCT crack propagation. As a result, they further concluded no convergence difficulties however in order to simulate crack propopgation, required intrinsic fracture properties (G_{Ic} etc.). Furthermore, VCCT has been proven to analyse buckling and delamination processes in composite structures [27] as well as already providing success in preliminary solutions to samples undergoing DCB and ADCB tests [14, 19, 39].

$$\begin{cases} G_I = \dfrac{1}{2\Delta a} R_y \Delta v \\ G_{II} = \dfrac{1}{2\Delta a} R_x \Delta u \end{cases} \tag{2.8}$$

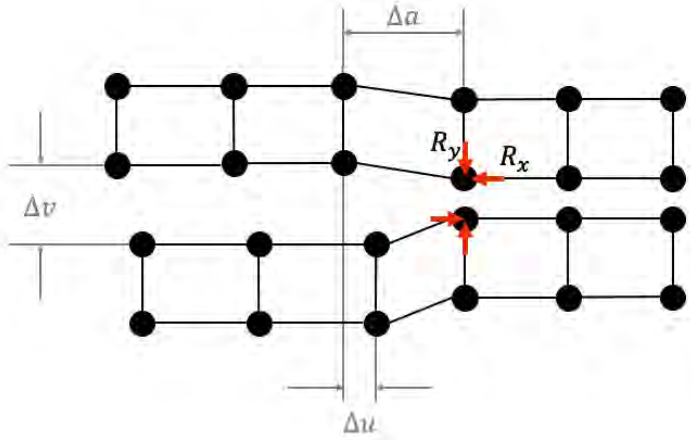

Figure 2.9: VCCT diagram

VCCT Model

To model the VCCT model, ANSYS Parametric Design Language (APDL) will be used due to its user-controlled interface. In order to ensure correct values, the sample will be modelled to the requirements listed under Section 2.3 with the material properties of the FML being previously outlined in Section 2.4.2. The samples will be modelled using two SOLID 185 8-node blocks at their respective substrate thickness'. The FML interface will be partially meshed allowing the model to begin debonding at the initial crack length of 47.5mm.

A refined mesh is defined in order to capture the information surrounding the crack tip, this has resulted in a maximum element size of 0.75mm (x coordinate) and 0.625mm (y coordinate) totalling to 19,803 nodes and 18,000 elements. The refined mesh is shown in Figure 2.10 indicating that the free end nodes will be completely fixed (allowing no movement in the x, y, z direction) with each substrate being displaced by 'd_y'; the vertical displacement as provided by the coordinate system.

It is important to realise the limitation in the VCCT FEM model presented here that due to having no known information regarding the intrinsic SERR 'G_c' values, crack propagation cannot be modelled. Therefore, the FEM model will be displaced once experimental testing has commenced. The deflection at failure (where crack propagation initiates) will then be input into the VCCT model for comparison.

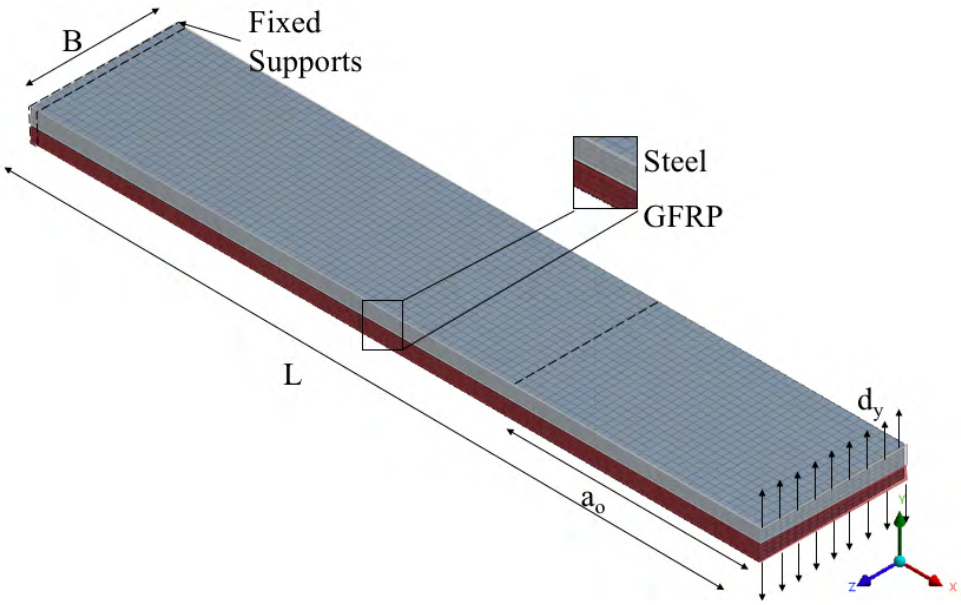

Figure 2.10: Finite Element Model mesh

2.6 Conclusion

A Literature Review has provided information in order to define the projects scope more clearly. Furthermore, it revealed:

1. The TSA measurement technique has previously been proven to provide simplicity in approximating mode I results to the conventional side view technique.

2. A GFRP-steel FML is of interest due each materials high use across a variety of industries. Furthermore, FMLs are of great interest as they overcome the limitations of each material constituent.

3. Delamination at the interface is the major concern in FMLs as it significantly affects the fracture properties. In addition, the surface treatment of each materials surface is critical to ensure ideal bonding has occurred.

4. DCB and ADCB are effective test procedures to determine mode I and mixed mode properties using TSA and side view measurement techniques. Furthermore, they provide simplicity as they are the same procedure, at varying material thickness'.

5. Both the TSA and side view measurement techniques rely on approximating the crack length upon delamination where they focus on the top and side surfaces of the sample respectively. This allows SERR values to be calculated.

6. FML mode I, consisting of 21 plies (2.184mm) of HexyPly 914 S-glass fibre sheets and 1mm of A366 steel will initially be tested. Following mode I, mixed mode consisting of 24 plies (2.496mm) of HexPly 914 S-glass and 8mm of A366 steel will be tested. This will allow a direct comparison to conclude if TSA and side view measuring techniques are capable of capturing the influence of mode II.

7. The VCCT FEM model will be used in order to further provide a basis of results to the experimental results. Furthermore, the model will provide simplicity in ensuring mode I and mixed mode values are theoretically occuring.

8. A strict manufacturing procedure is required when manufacturing the FML in order to avoid pre-mature failures and non-ideal bonding between the materials.

9. Strain Energy Release Rates (SERR) can be physically interpreted as the amount of energy required in order to break the atomic structure of a material, or in this case the interface.

Chapter 3

Fibre Metal Laminate Manufacturing

This chapter outlines the manufacturing procedures of the GFRP-steel FML. The procedures are categorised below and are required to be carried out in the order presented:

1. GFRP Manufacturing Procedure.
2. GFRP & Steel Surface Treatment Procedure.
3. GFRP & Steel Bonding Procedure.
4. FML Water Jet Cutting & TSA Preparation.

Furthermore, the manufactured FML samples are then assessed through the use of microscopy to inspect the quality of the bonding between the interfaces with a discussion and results outlining any areas of concern.

3.1 Manufacturing Procedures

The following equipment and apparatus of the procedures carried out are listed in Table 3.1.

3.1.1 GFRP Manufacturing Procedure

The following section describes the procedures undertaken to produce the GFRP composite panels previously prepared by Kurt Mills [5]:

1. The first GFRP prepreg sheet was removed exposing the epoxy. The epoxy side then faced upwards on an acrylic plate ensuring the corners of the sheet aligned to the plate.
2. The following prepreg coverings was removed allowing the GFRP sheets to be bonded together. Each layer was then de-bulked by applying pressure with the roller to ensure no air was present between the layers.
3. For each of the layers required, the previous step was applied ensuring correct the corners of each previous GFRP sheet was aligned.
4. A sheet of release film was then applied over the final pre preg sheet followed by a sheet of peel ply as indicated in Figure 3.1a and Figure 3.1b.

(a) GFRP release film applied (b) GFRP peel ply applied

Figure 3.1: Applying plastic and release films in GFRP manufacturing

5. A layer of 'breather cloth' was then placed over the final peel ply layer followed by a vacuum bag film placed over the entire plate as shown in Figure 3.2. The breather cloth allowed to trap and hold the excess resin from the laminates. The vacuum bag film was cut to size to such that there was approximately 100mm excess in each direction. One side of the white protective tape surrounding the outside of the vacuum bag film was then removed.

Figure 3.2: Vacuum bagging application for GFRP manufacturing

6. A small insert was cut for the vacuum line with all of the remaining white protective tape removed to complete the sealing of vacuum bag to the plate. This allowed for an air-tight seal and is shown in Figure 3.3.

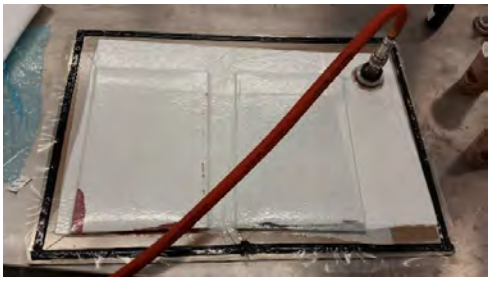

Figure 3.3: Vacuum bagging GFRP manufacturing

7. The vacuum pump was then turned on to provide suction and allowed the laminates to cure at room temperature overnight.

3.1.2 GFRP & Steel Surface Treatment Procedure

Before bonding the GFRP and steel substrates together, it is required that solution be prepared in order to successfully carry out the surface treatment procedure.

Solution Treatment Preparation

1. 1g of Epoxy Silane was added to each 100ml of distilled water (1% by weight solution) into a large clean beaker and was mixed for a total of one hour with an electric stirrer. Enough solution was prepared such that each 1mm and 8mm steel panel was able to be completely submerged in the required step as later indicated. This resulted in 2L of solution being required for each panel.

Surface Treatment Procedure

Following the Solution Treatment Preparation process, the Surface Treatment Procedure was carried out and included:

1. Using separate P180 aluminium oxide sandpaper, the bonding surface of the steel and GFRP was abraded first in the length direction followed by the width direction until a uniform finish was achieved.

2. The 'to be' bonded surfaces were then wiped down with acetone soaked tissues followed by deionised water soaked tissues until no material deposits were able to be identified on the tissues.

3. The surfaces were then submerged in a layer of deionised water to ensure that there were no water breaks (confirming no particle matter). Note that if water breaks were present, steps 1 - 3 of the Surface Treatment Procedure was repeated.

4. After the 1 hour of mixing, the Epoxy Silane and distilled water from the Solution Treatment Preparation was then poured into a large container where only the steel panels were submerged for a total of ten minutes, this is indicated (showing only the 1mm steel panel) in Figure 3.4.

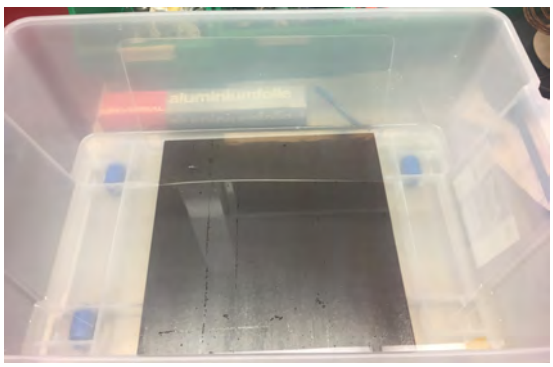

Figure 3.4: Submerged steel panel in epoxy silane/distilled water solution

5. Both the GFRP and steel panels were then placed into the oven and dried at 110° for one hour. Note that once removed from the oven, bonding must occur within one hour. Failing to do so will result in the entire process being repeated.

3.1.3 GFRP & Steel Bonding Procedure

Following the surface preparation and treatment procedures, the following procedure outlines the steps taken in order to bond the GFRP and steel panels together to produce the FML and include:

1. On the 'to be' prepared steel panel steel surface, using the release film, a pre-crack was inserted with 80 µm teflon tape providing the necessary bondline thickness along the outer edges at approximately 47.5mm. Heat resistant tape was then applied for reinforcement to hold the film and teflon tape in place as indicated in Figure 3.5

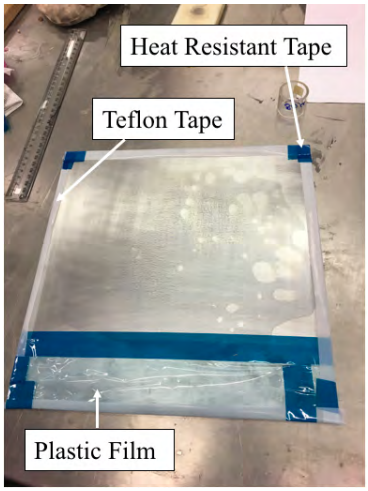

Figure 3.5: Steel pre-crack insertion

2. The Loctite 9394 was then mixed at a ratio of 100/17 (Part A/B) by weight in a plastic cup using a popsicle stick. The epoxy was then mixed thoroughly until a uniform colour and consistency was achieved.

3. Using the QEP V-notch adhesive floor spreader as indicated in Figure 3.6, the epoxy was applied to both the GFRP and steel panel surfaces prior to mating. Note that the geometry of the applicator is of great importance in applying an even layer of material without entrapping air.

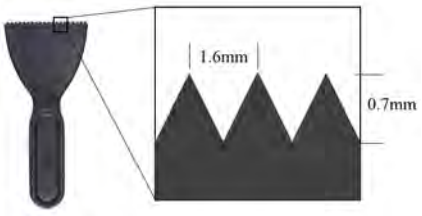

Figure 3.6: Applicator geometry and importance in FML bonding procedures

4. The epoxy was then applied to both surface treated panels ensuring a thin, even layer was achieved before bonding as seen in Figure 3.7.

5. The panels were then mated together in the hot-press at a temperature of 70°C with a force of 1.24 kN for four hours. A thermocouple and force gauge assisted in confirming the required values as indicated in Figure 3.8.

3.1.4 GFRP-Steel Water Jet Cutting & TSA Preparation

Following the bonding procedure, Water jet cutting and TSA preparation is required.

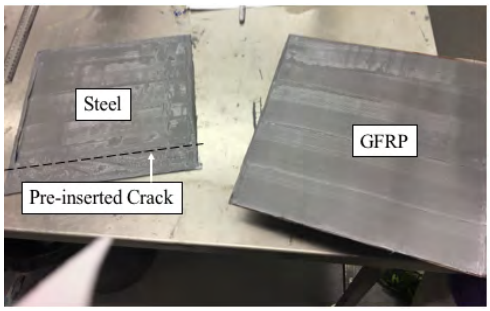

Figure 3.7: Epoxy applied to both the GFRP and steel panels

Figure 3.8: FML composite bonding in the hot-press

Water Jet Cutting Preparation

1. The plates required water-jet cutting in order to have the required dimensions therefore, A .DXF file was created. The layout is indicated in Figure 3.9 indicating a total of seven test samples, one interface inspection sample (to comment on the quality of the bonding procedure) as well as four material inspection samples. In order to ensure a quality bond between the interfaces, a 25mm limit was placed from each edge as indicated as grey dashed lines.

TSA Preparation

Once the samples have been cut, the TSA preparation is required, this includes the following steps:

1. Sticky tape was applied to the top surface (GFRP) where the loading blocks are to be placed.

2. A speckle pattern was then applied to the GFRP surface by carrying out a first layer of white spray paint followed by a light application of the black spray paint. This is indicated in Figure 3.10.

3. Once the paint has dried, the sticky tape was removed and the loading block areas were sanded using the P180 aluminium oxide sandpaper, cleaned using paper towels

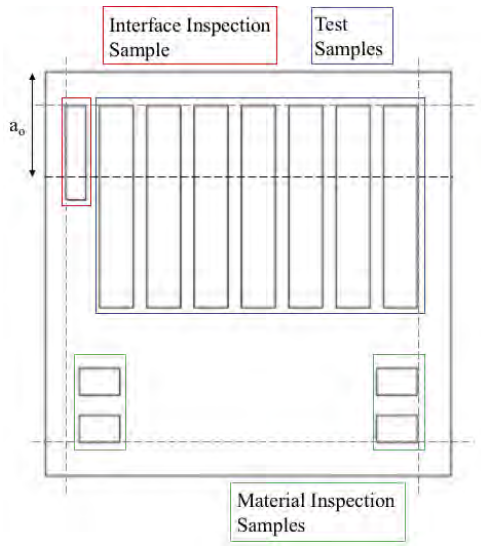

Figure 3.9: DXF Water-jet diagram

Figure 3.10: Speckle pattern applied to the samples

with water followed by acetone surface cleaning. The same process was repeated on the loading blocks.

4. A Loctite 3421 cartridge was then placed into the adhesive applicator gun. Using the applicator gun, an even amount of epoxy was applied to the surface of the loading blocks such that they may provide adequate bonding to the surfaces. Note to ensure that the holes of the bonding blocks are placed facing along the width of the specimen to allow for it to be input into the INTSTRON testing machine.

5. The bonding blocks were then clamped to the samples and allowed to cure for a total of 48 hours. After the first 24 hours, the clamps were removed and the samples were placed in isolation to continue curing. The initial 24 hour bonding is provided in Figure 3.11.

3.2 Microscopy / Inspection and Discussion

3.2.1 Microscopy / Inspection

A series of microscopy and inspections has been conducted on both the mode I and mixed mode FML interfaces and pre-cracks. These inspections have revealed a number of concerns that may further impact the results. In reference to all the microscopy images, the top side reflects the steel with the grey middle section being the 9394 Loctite Epoxy

Figure 3.11: Clamps applied to the samples to bond the loading blocks

between the steel and GFRP substrates. The pre-crack images show the VACPAK A6200 release film with a scale indicating the epoxy interface thickness ranging between 400 µm to 450 µm.

Figure 3.13b indicates the 8mm steel panels surface roughness at the pre-crack varying within 100 µm. The mixed mode interface in Figure 3.13a indicates localised corrosion along its edges compromising the bond between the epoxy and steel surface. The Mode I interface provided in Figure 3.12b indicates the ideal bonding case between the two substrates with Figure 3.12b showing corrosion growing over the release film.

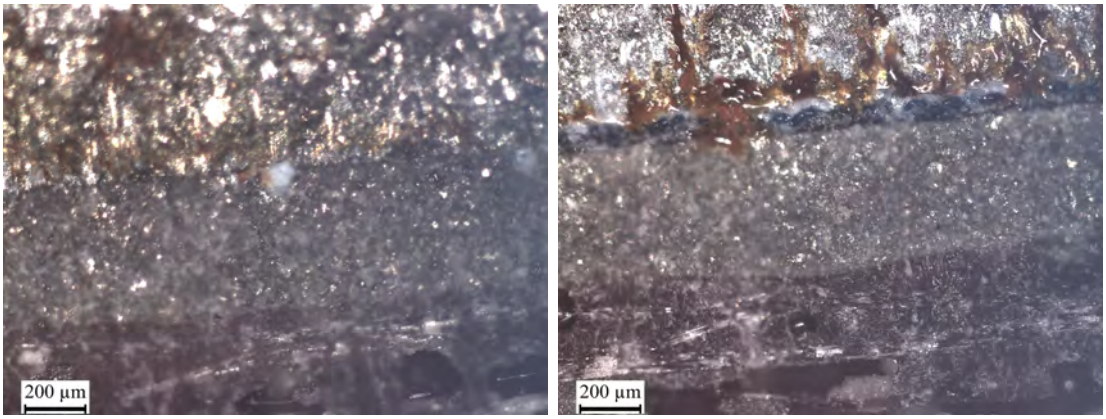

(a) Mode I interface (b) Mode I pre-crack

Figure 3.12: Microscopy mode I inspection results

Figure 3.14 indicates that the water jet cutting has impacted the mode I interface only. This has resulted in small void like openings along the samples edges. The voids along the interface suggest that it is due to the contribution of:

1. The steel panels rough surface causing non-ideal bonding between the interfaces. This can can be seen more clearly when conducting the manufacturing of the samples (see Figure 3.4). If future manufacturing is to occur, sand blasting is to be conducted on the steel samples to remove all rust from the surface and ensure an ideal bonding scenario.

2. Due to the consistency of the voids present along the width and with the edge voids not being present on the larger mixed mode samples, this has been caused from the

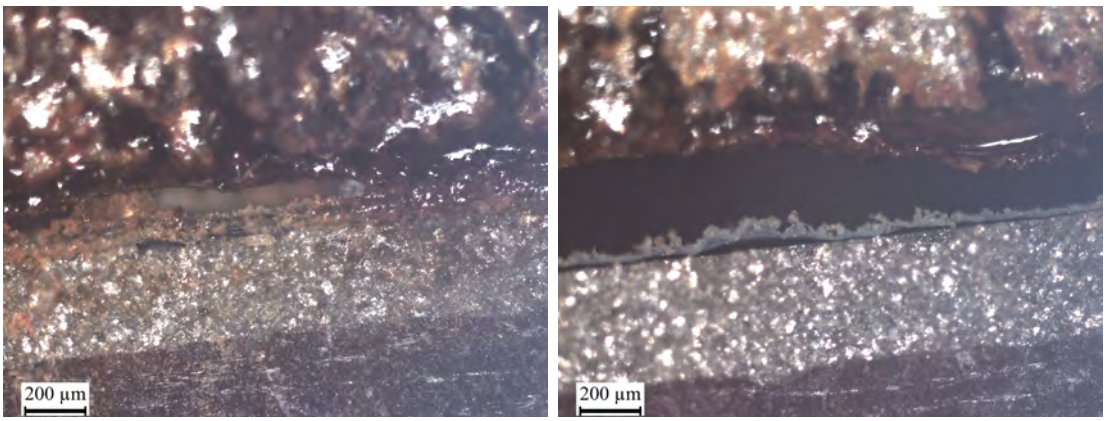

(a) Mixed mode interface (b) Mixed mode pre-crack

Figure 3.13: Microscopy mixed mode inspection results

water jet-cutting. As the panel is impacted and begins to vibrate, water has dispersed and struck along the thickness of the sample causing damage to the interface. The inspection revealed that the voids along the edge seem to not penetrate into the sample however, this will result in pre-mature detection when conducting the side view measurements along the side in comparison with the middle of sample.

Failing to remove the localised rust from the steel panels as well as the water-jet cutting may further indicate an impact to the results as voids typically create unpredictable behaviour due to; acting as stress concentrators, allowing moisture to penetrate into the interface and overall, leading to a decrease in performance by up to 20% to the expected results [18]. It is therefore of concern that the interfaces across both samples have been compromised and may lead to a variation in results.

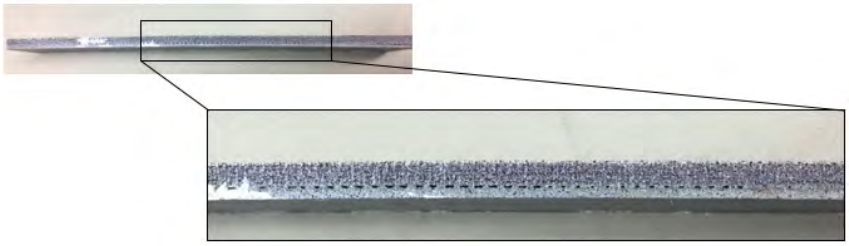

Figure 3.14: Voids present along the mode I interface

3.2.2 Discussion

From the water jet cutting, the overall samples are 23mm in width which has caused issues in bonding and clamping the 25mm loading blocks to the samples evenly. In addition, Figure 3.15 indicates that from the initial unconstrained clamping, the loading blocks were able to move which would result in mode III SERR values. To rectify the issue, a jig was set-up to ensure correct lining along the width of the specimen as previously described in Figure 3.11.

Initially, Loctite Double Bubble [30] was used as the bonding agent to combine the loading blocks to the specimens. However, it was later inspected and shown to not be sufficient for the strength requirements and from an initial test, premature failure occurred before the INSTRON machine reached the pre-inserted crack. This led to Loctite 3421

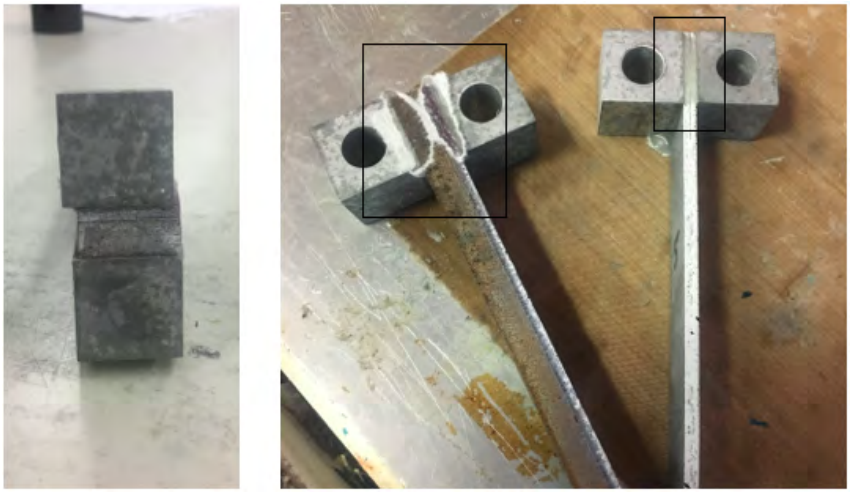

Figure 3.15: Initial bonding block issues

to later be used as mentioned in the above procedures due to its increased mechanical properties and ability to correctly bond the aluminium loading blocks to the steel and GFRP surfaces. Furthermore in respect to the pre-test, premature failure was also identified and was caused from bonding the loading blocks to parts of the speckle pattern when clamping. This resulted in the speckle pattern being torn off the samples surface along with the loading blocks. To mitigate this, a layer of tape was applied when applying the speckle pattern to ensure the GFRP top surface is free from spray paint for where the loading blocks are to be bonded.

3.3 Conclusion

Overall, the manufacturing process of the Fibre Metal Laminates outlined in this chapter suggests:

1. The procedures outlined in this chapter are to provide an effective means in manufacturing FMLs.

2. The teflon tape, plastic film and heat resistant tape were capable of creating a pre-crack between the FML samples. This will successfully make it achievable to identify when loading the samples that the pre-crack has been reached, corresponding to a 'peak' in force.

3. The latter used Loctite 3421 epoxy used in conjunction with the provided clamping procedure was capable of bonding the loading blocks to the samples as well as ensuring minimal mode III SERR values.

4. From the microscopy images, there is concern that the mode I and mixed mode interfaces have been compromised. This may further impact the results when carrying out the tests leading to incorrect SERR values.

5. The mode I interface has been impacted with water when water-jet cutting the samples. This has resulted in voids along the edges which will further cause premature approximation of the crack length when conducting the tests using the side view measuring technique.

Table 3.1: Apparatus of procedures

Procedure	Apparatus
1. GFRP Manufacturing	21x HexPly 914 S-glass (Twill weave) panels (300 x 300mm) [31] 21x HexPly 914 S-glass (Twill weave) panels (300 x 300mm) [31] 360g (5:1 Ratio) Epoxy (300g Epoxy, 60g resin) [31] Application brush (paint brush) VACPAK A6200 ETFE/fluropolymer release film [6] Breather cloth Acrylic plate Roller Vacuum bag Vacuum pump
2. GFRP & Steel Surface Treatment	**Solution Treatment Equipment** Beaker (enough to contain 2L of solution) Container to submerge the A366 steel panels Epoxy silane [47] Distilled water Electric stirring machine (incl. electric stirrer) **Surface Treatment Equipment** P180 aluminium oxide sandpaper Acetone [11] Tissue paper / paper towels Composite curing oven capable of 110°C
3. GFRP & Steel Bonding	1mm steel of A366 steel thick panels (300 x 300mm) [49] 8mm of A366 steel thick panels (300 x 300mm) [49] Popsicle stick Loctite EA 9394 epoxy paste adhesive [37] QEP 75 x 1.6mm V-notch adhesive floor spreader [2] VACPAK A6200 ETFE/fluropolymer release film [6] Mylar heat resistant tape [3] 80 µm teflon tape [4] Hot press composite machine
4. FML Water Jet Cutting & TSA Preparation	**Water Jet Cutting** .STL file (required to cut the sample) Water jet cutter **TSA Preparation** White and black spray paint Loading blocks (L x W x H) - (25mm x 25mm x 25mm) Loctite 3421 Hysol epoxy adhesive [36] (to attach the loading blocks) Epoxy applicator gun [22] Acetone Tissue paper / paper towels Popsicle stick P180 aluminium oxide sandpaper Sticky tape Clamps

Chapter 4

ARAMIS (TSA) & Side View Setup

Before carrying out the experimental tests on the prepared FML samples, the ARAMIS machine requires calibration such that the TSA technique provides accurate measurements. The steps include:

1. Preparation - as outlined previously in Section 3.1.4.
2. Pre-processing - the calibration procedure to ensure the speckle pattern is able to be identified using the ARAMIS software.
3. Post-processing - the calculations and analysis of data results.

4.1 ARAMIS (TSA) & Side View Pre-processing

The following steps outline the procedure required to calibrate the ARAMIS machine for TSA to be applied. This includes:

1. 2x 12mm camera lenses were selected due to increasing the allowable aperture.
2. In knowing the measuring volume required (constrained by the specimen size), the ARAMIS manual revealed the requirements as indicated in Table 4.1. This resulted in a facet size of 19 x 19 pixels with a facet distance set to 16 pixels creating an overlap of 3 pixels with each neighbouring facet.

Table 4.1: ARAMIS (TSA) calibration requirements

Description	Value
Lens (mm)	12
Measuring Volume (mm x mm)	200 x 170
Min. Length Camera Support (mm)	500
Measuring Distance (mm)	320
Camera Slider Distance (mm)	104
Camera Angle (°)	25
Calibration Board (mm x mm)	CP20 250 x 200

3. The camera slider distance and angles as well as measuring distances were then adjusted on the ARAMIS machine before calibration was carried out using the CP20 250mm x 200mm board as indicated in Figure 4.1. The following steps were required:

- First, the laser pointer was lined up to the centre of the calibration board at an angle of 0° to begin the set-up.
- Calibration was then conducted by rotating the board to an angle of 40° where the ARAMIS laser pointer was lined up to the centre of the board with the camera on the computer screen lining up the cross hairs.
- This was carried out a total of four times (each rotation) to calibrate ARAMIS.

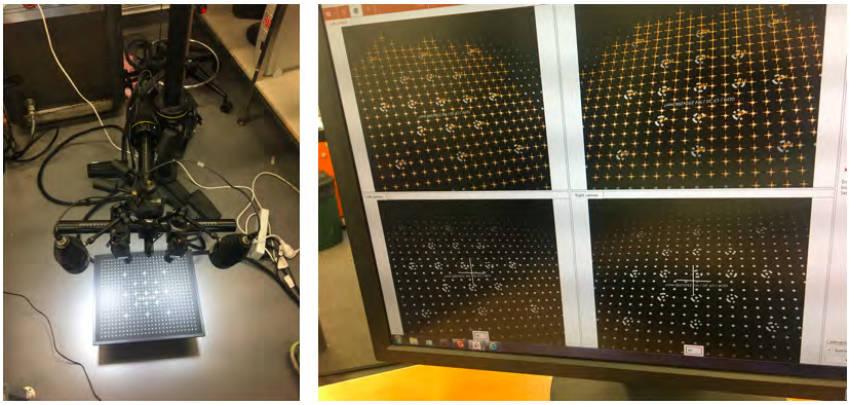

Figure 4.1: ARAMIS calibration

4. Once the calibration was successful, the ARAMIS machine was then relocated around the INSTRON machine using a 100kN loading block.

5. The distance calibrated was then measured between the specimen and the two 12mm camera lenses to ensure correct focus. The side view camera was then superimposed underneath the ARAMIS machine to ensure there was no viewing restriction. The final set-up is indicated in Figure 4.3.

6. The ARAMIS machine was input to measure at 1 Hz until reaching the pre-crack. Once reached, ARAMIS was input to measure at 0.5 Hz for the remainder of the test. The ARAMIS (TSA) identification is provided in Figure 4.2 with left image indicating the identified surfaces before testing is to commence and right indicating the identified plane surface that has to be manually selected before testing.

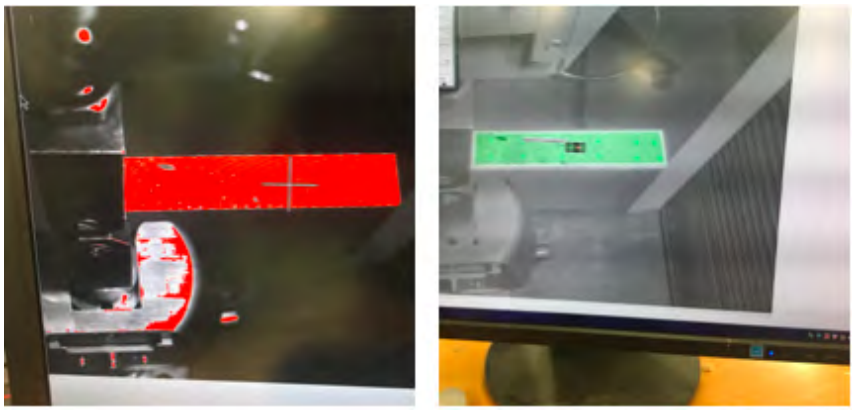

Figure 4.2: ARAMIS (TSA) computer display

7. The ARAMIS (TSA) and side view measuring techniques were then initiated followed by the INSTRON machine and testing commenced.

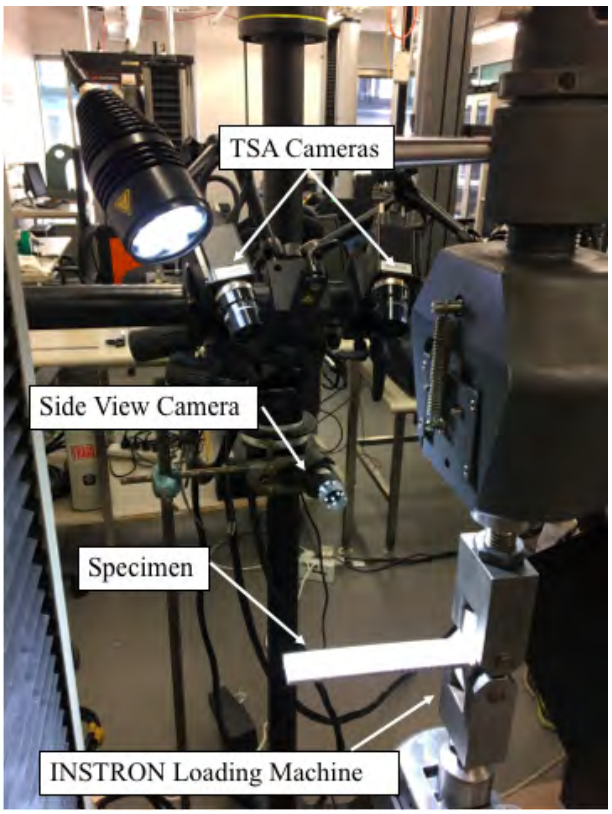

Figure 4.3: ARAMIS / side view and INSTRON test schematics

4.2 TSA Post-processing

Following the experiments, post-processing is separated into two relevant sections:

1. TSA Procedure - outlining the steps undertaken to produce TSA results using the ARAMIS machine.

2. Methodology - providing the information to how the data is manipulated to produce and present information.

4.2.1 TSA Procedure

The following procedure has been used in order to extrapolate the distances between the selected points using the ARAMIS software. It is recommended that the procedure be read in conjunction with Figure 4.4 (refer page 32).

1. Beginning at the initial stage (time of zero seconds), the entire surface component was selected before DCB testing commenced. This was to ensure that the entire component was captured in order for each point to be updated.

2. A coordinate system was constructed on the free-end of the surface (at the initial stage). The z coordinate was also made to ensure that it was positive in the upwards direction.

3. A reference plane (3 point plane) was then selected at the last stage (premature to complete failure) and placed on the free-ends most horizontal section. This is required as the reference plane will update and calculate the distances between each selected point. By constructing the reference plane on the latest stage, it is assured that the most horizontal section has been selected throughout the entire test.

4. A perpendicular plane was then constructed (at the initial stage) across the length of the specimen. The perpendicular plane was then selected to be orthogonal to the reference plane.

5. On the last stage (before complete failure) four section planes were created evenly along the width and referenced to the perpendicular plane. This provides the surface for where points are able to be selected.

6. Points were then manually selected along each section plane and measured to the reference plane. A total of five points were selected in close proximity to the pre-crack such that estimates of crack length 'a' were able to be measured at initiation and steady state.

7. Distances were then created (project point distances) that measure the difference in displacement between the reference plane and each selected point (with respect to coordinate system previously defined).

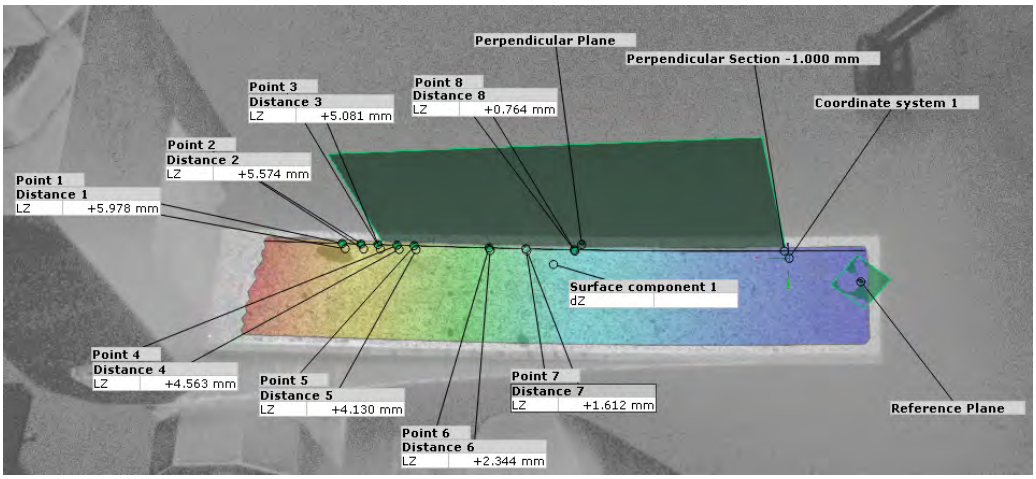

Figure 4.4: TSA raw information procedure

4.2.2 Methodology

In order to determine the the vertical displacement 'd_z' of the samples top surface using the ARAMIS software, the sample is distributed evenly into four section planes along its width as provided in Figure 4.5. Along each section plane, individual points are created to measure the vertical displacement throughout the test. This allows each point to be updated with respect to the Reference Plane. The displacement contours are indicated by colour representing the % relative displacement difference between the Reference Plane. Note that in Figure 4.5, the crack length is approximated within the zone of the blue and cyan contours.

In order for the TSA measurement technique to provide the necessary information to calculate SERR values, each individual point is plotted with respect to displacement and time to approximate the crack length location. The displacement 'd_z' at the initial pre-crack point is then updated as the sample extends (provided by ARAMIS). The ARAMIS time frame is then synced with the INSTRON time frame in order to extract the corresponding force 'P'. Figure 4.6 provides each individual point (five points in total for simplicity) beginning to be displaced as the crack length increases. Note that point 1

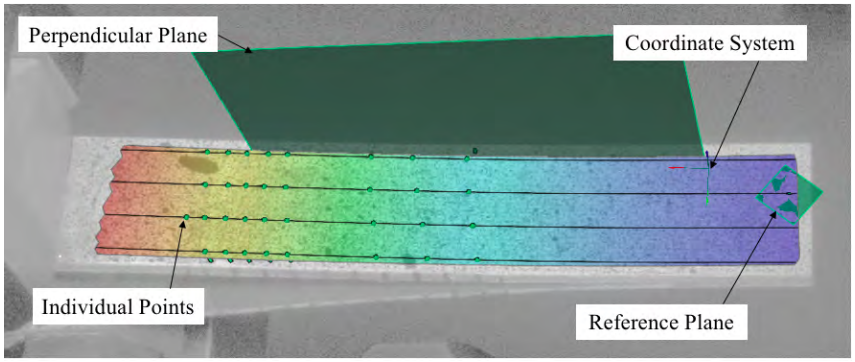

Figure 4.5: TSA post processed information

corresponds closest to the loading blocks with point 5 being the furthest.

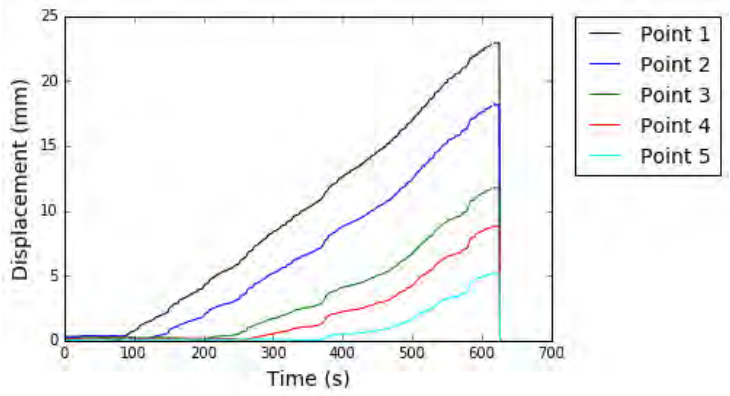

Figure 4.6: TSA point displacements

The side view measurement technique follows the same methodology to that of TSA in extracting SERR values, however relies on the INSTRON machine to supply the force values *and* displacement '*d*'. In addition, the crack length is approximated by black markings along the samples width as indicated in Figure 4.7.

Figure 4.7: Side view crack length approximation

Figure 4.8 provides the methodology in processing the results using the ARAMIS (TSA) and side view measuring techniques utilised in conjunction with the INSTRON test machine. As the two techniques and ARAMIS machine correspond to their own time frames however, a local time frame is required in order to obtain the accurate force and displacement values.

Python, a numerical method software program provides simplicity in extracting and displaying information. Included in the *Python* numerical analysis, a Median filter is applied to reduce noise feedback, all in efforts to further approximate the crack length. From approximating the crack length to a corresponding force and displacement, SERR

values can be calculated using the Modified Beam Theory and J-integral reduction schemes as discussed in the next chapter.

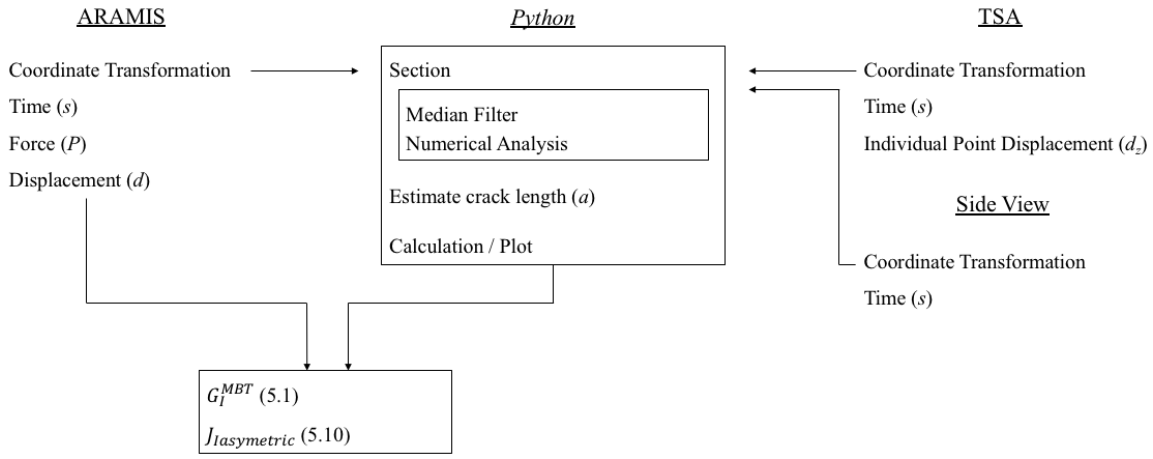

Figure 4.8: Post-processing flowchart

4.3 Discussion

4.3.1 Pre-processing Discussion

The major contributing issue with the calibration procedure included the artificial lighting in the room where the testing was being conducted. This resulted in complications in ARAMIS failing to identify the points on the calibration board (refer Figure 4.2). By adjusting the ARAMIS lights however, this was able to be mitigated.

Once calibration was successful, ARAMIS was subject to sensitivity issues due to requiring the overall magnitude in length to be approximately equal to the values listed previously in Table 4.1. A simple approach to rectify the issue was found to place a ruler from the sample to ensure the correct length.

4.3.2 Post-processing Discussion

TSA

Initially, the surface component (step 1) was selected at a later stage however, it was found to be more efficient in capturing the entire surface component at the initial stage before testing had commenced. This led to a decrease in overall processing time as once selected, ARAMIS will update the surface component to all the remaining stages. In selecting a later stage and attempting to update back to the initial stages, ARAMIS had instability issues and was not able to accurately capture the top surface component successfully.

One of the major setbacks comes from ARAMIS lack of coding manuals. This led to the procedure of manually selecting and measuring points of interest along the sample restricting the full benefits of the TSA method. Once a procedure is discovered however, this has the opportunity to streamline extracting information.

Methodology

Previously, a *Python* code originally created by Reiner et al. [45] was to be implemented to extract the information for the TSA and side view measurement techniques as well as the INSTRON machine. In order to produce the information through the *Python* code however, it involves additional ARAMIS software and experimental testing knowledge. This led to its abandonment leading to the methodology approach provided above.

The major limitation in the procedure carried out is ensuring a local time frame between the INSTRON machine with the TSA and side view measurement techniques. This required additional steps to manually sync to a respective time frame and therefore, relied heavily on the skills of the user. However, ARAMIS has been previously proven to supersede these time frame issues by connecting all the INSTRON machine and side view measurement technique to the ARAMIS (TSA) software [45].

4.4 Conclusion

The results of the processing and methodology approach suggest that:

1. The ARAMIS software is capable of measuring the deflection of the top surface of the sample thus being able to approximate the crack length required to calculate SERR values. In addition, the speckle pattern applied was able to be identified using the software indicating success.

2. The ARAMIS software is subject to sensitivity issues due to lighting however provides a major advantage in calculating the distances of any point of interest on the samples top surface. In addition, its lack of a programming manual has lead to the ad-hoc method of manually selecting points and therefore relies heavily on the skills of the user.

3. Additional efforts are required to implement the TSA measurement technique in regard to its side view counterpart however, comes at the reward of providing individual displacements at any point of interest.

4. Due to ARAMIS' instability issues, it is of great importance to define the reference and perpendicular planes, coordinate systems and top surface at specific stages outlined in the TSA procedure.

5. *Python* provides simplicity in calculating SERR values from the TSA and side view crack length measurements. Furthermore, it allows simplicity in applying a median filter to the raw data in efforts to assist in approximating the crack length location.

Chapter 5

Reduction Schemes

This chapter outlines the reduction schemes that are to be used in extracting the information from the INSTRON test machine and explains how SERR values may be calculated from approximating the crack lengths. It further provides the derivations such that an understanding may be developed between each respective reduction scheme to calculate SERR values and explain the variation in results once the samples have been tested. Two reduction schemes have been selected based on their success in producing values. The reduction schemes include:

1. The Modified Beam Theory.
2. The J-Integral.

5.1 Reduction Scheme: Modified Beam Theory

The ASTM D5528 [23] provides the method to calculate mode I energy release rates using the DCB test procedure (refer to Figure 2.4). As previously mentioned, it recommends a loading rate between 0.5 - 5 mm/min as well as to assess the results using the Modified Beam Theory reduction scheme as it yields the most conservative values. Equation 5.1 states the Strain Energy Release Rate (SERR) for Mode I.

$$G_I = \frac{3P\delta}{2B(a + |\Delta|)} \tag{5.1}$$

Where:

- 'P' equals to the applied load;
- 'a' refers to the crack length;
- 'δ' equals the load point displacement;
- 'B' is the samples width; and
- 'Δ' being the correction factor.

The Correction Factor 'Δ' is required as it takes into account rotation at the crack tip. In order to calculate this factor, a least squares plot of the cube root of the compliance (where $C = \frac{\delta}{P}$) as a function of delamination length is required as indicated in Figure 5.1 [23]. The deflection of the specimen is calculated by beam theory and is provided in Equation 5.2 [32].

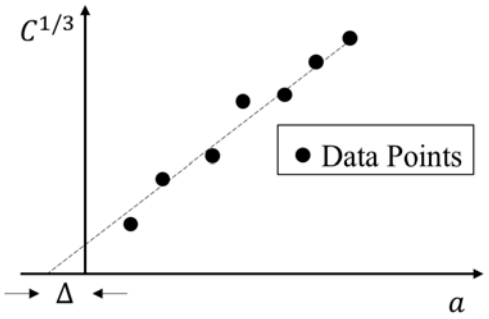

Figure 5.1: MBT correction factor diagram

$$\delta = \frac{P^3 L}{3EI} \tag{5.2}$$

Where:

- 'E' refers to the samples Young's modulus;
- 'L' equalling the samples length; and
- 'I' referring to the samples area moment of inertia.

5.2 Reduction Scheme: J-Integral

The Elastic Plastic Fracture Mechanic (EPFM) technique, the J-integral is well suited for assessing both mode I (DCB) and mixed mode (ADCB) experiments. Its ability to calculate mixed mode SERR values is by defining a path-independent line integral around the crack tip [44]. The J-integral is defined by Equation 5.3 and visually in Figure 5.2 [26, 42].

$$J_I = \int_C \left[W dy - \sigma_{ij} n_j \frac{\partial u_i}{\partial x} ds \right] \tag{5.3}$$

Where:

- 'W' refers to the strain energy density. This is the energy caused from displacing the specimen;
- 'C' explaining the line integral surrounding the crack tip;
- 'σ_{ij}' defines the stress tensor with the associated stress defined across 3 dimensions where
- 'i' defines the direction in which the stress acts and 'j' the orientation of the surface on which it acts upon (x, y, z);
- 'n_j' describing the normal unit vector around the contour at any incremental value 'ds';
- 'x, y' stating the co-ordinate system at the base of the crack tip; and
- 'u' referring to the resulted displacement as the specimen begins to be pulled apart.

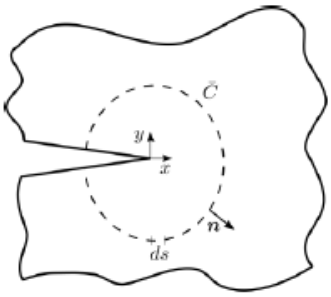

Figure 5.2: J-Integral along a path independent integral 'C' [45]

The following methodology has been extracted from Reiner et al. [45]. The equation developed has been derived for a mode I DCB test case. It will then be adapted to suite the mixed mode ADCB FML test procedure required in order to approximate SERR values.

Taking into consideration the top substrate of the DCB sample, the contour 'C' is applied around the four sections surrounding the crack tip as indicated in Figure 5.3.

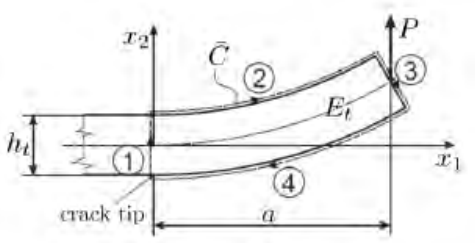

Figure 5.3: Top section of DCB substrate for J-integral [45]

The vertical deflection at any length '$u_2(x_1)$' along the specimen is provided by Equation 5.4 with the axial displacement '$u_1(x_1, x_2)$' described in Equation 5.5.

$$u_2(x_1) = \frac{Px_1^2}{6EI}(3L - x_1), \qquad 0 \leq x_1 \leq L \tag{5.4}$$

$$u_1(x_1, x_2) = -\frac{P}{2E_tI_t}(2ax_1^2 - x_1^2)x_2, \qquad u_2(x_1) = \frac{P}{2E_tI_t}(ax_1^2 - \frac{x_1^3}{3}) \tag{5.5}$$

The first term in Equation 5.3, 'Wdy' is evaluated through the thickness direction 'dx_2' with respect to each four contours. In knowing the specimen is fixed at the length of 'x_1' equalling zero, only contour number three requires to be calculated. As previously discussed, the shear stress '$\sigma_{xy} = \sigma_{12}$' corresponds to the shear stress measured and therefore; $\sigma_{xy} = \frac{P}{Bh_t}$. Applying the constraints ($x_1 = 0$), Equation 5.6 provides the outcome to the strain energy density term.

$$\begin{cases} \int W dx_2 = \int \frac{1}{2} \sum_{i=1}^{2} \sum_{j=1}^{2} \sigma_{ij} \epsilon_{ij} dx_2 \\ \qquad \downarrow \\ \frac{1}{2} \int \sigma_{12} \epsilon_{12} dx_2 \\ \qquad \downarrow \\ \frac{1}{2} \int \sigma_{12} \left(\frac{\partial u_2}{\partial x_1} + \frac{\partial u_1}{\partial x_2} \right) dx_2 \\ \qquad \downarrow \\ \frac{1}{2} \frac{P}{Bh_t} \frac{P}{2E_t I_t} \int (2ax_1^2 - x_1^2 - 2ax_1 + x_1^2) dx_2 = 0 \end{cases} \tag{5.6}$$

Considering the second term of Equation 5.3, the '$\sigma_{ij} n_j \frac{\partial u_i}{\partial x_1}$' term is expressed in Equation 5.7.

$$\begin{cases} \int_C \sigma_{ij} n_j \frac{\partial u_i}{\partial x_1} ds = \int_{h_t/2}^{-h_t/2} \sigma_{21} \frac{\partial u_2}{\partial x_1} dx_2 \Big|_{x1=a} \\ \qquad \downarrow \\ \int_{h_t/2}^{-h_t/2} \frac{P}{Bh_t} \frac{P}{2E_t I_t} (2ax_1 - x_1^2) dx_2 \Big|_{x1=a} \\ \qquad \downarrow \\ \frac{P^2}{2Bh_t E_t I_t} (2ax_1 - x_1^2) \Big|_{x1=a} \int_{h_t/2}^{-h_t/2} dx_2 \\ \qquad \downarrow \\ \frac{12P^2a^2}{2B^2h_t^3E_t} \end{cases} \tag{5.7}$$

In combining the terms from Equations 5.6 and 5.7, the J-integral for the top surface 'J_t' in plane stress is provided in Equation 5.8. Note that plane stress is assumed for the calculations due to the specimens thickness.

$$J_t = \frac{12(Pa)^2}{2B^2h_t^3E_t} \tag{5.8}$$

Therefore, for a symmetric case, mode I SERR is simply provided in Equation 5.9. For the asymmetric case, the Young's Modulus and height must be taken into consideration and therefore, the top (t) and bottom (b) substrates are provided. The asymmetric mode I SERR is provided in Equation 5.10.

$$J_{Isymmetric} = 2J_t = \frac{12(Pa)^2}{B^2h_t^3E_t} \tag{5.9}$$

$$J_{Iasymmetric} = J_t + J_b = \frac{12(Pa)^2}{2B^2} \left[\frac{1}{h_t^3E_t} + \frac{1}{h_b^3E_b} \right] \tag{5.10}$$

Note that throughout the rest of this project, '$J_{Iasymmetric}$' will simply be referred to as 'J_I'.

Chapter 6

Mode I FML Analysis

Before carrying out the mixed mode FML testing. A mode I test experiment is initially required in order to:

1. Assess the results across the expected mode I analysis. Due to equating the compliance in each substrate provided in sections earlier (Section 2.4.2), a mode I Strain Energy Release Rate (SERR) value is expected.

2. This will therefore allow a quantifiable comparison when carrying out the mixed mode FML tests or rather, the affect mode II has on mixed mode loading and whether TSA and side view measurement techniques are able to distinguish between the samples. Furthermore, the FEA VCCT model will be applied at the expected deflection at which crack propagation initiated and compared to the results.

Following the results, a discussion is provided where each of the mode I samples are compared indicating trends in the results, the success in the manufacturing procedure as well as confirmation/rejection of the concerns raised in previous sections.

6.1 Mode I Interface Characterisation

The mode I FML has previously been manufactured making up of 21 sheets (2.184mm total) of HexPly 914 S-glass and a 1mm steel panel. This has resulted in a total thickness of 3.32mm once bonded together with a pre-inserted crack of 'a_o' equal to 47.5mm. Each sample has a total length of 150mm and width of 25mm. The DCB experiments were conducted at a room temperature of 24°C and 58% humidity at a loading rate of 2.5 mm/min. The INSTRON machine provided a time, displacement and force output with the ARAMIS (TSA) measurement technique recording at 1 Hz until reaching the pre-crack. Once reached, ARAMIS was updated to measure at 0.5 Hz for the remainder of the test as previously outlined in Section 4.2.2.

Load-displacement curves assist in indicating the materials compliance as the crack extends along the FML interface. Due to time constraints however, only two mode I FML samples were able to be tested. Referring to the load-displacement curves in Figure 6.1, consistent delamination occurs at approximately 60N indicating success in the pre-crack manufacturing procedure with sample 1 at a displacement of 1.9mm and sample 2 at 3.5mm. Sample 2 shows an initial load peak at 107N and is explained by the Loctite 3421 bonding the pre-crack when clamping the bonding blocks to the sample. Furthermore, a saw-tooth type response is indicated in sample 2 as the crack begins to extend along

the FML interface. This however is absent for sample 1 suggesting non-ideal bonding has occurred and is later discussed (refer Section 6.4).

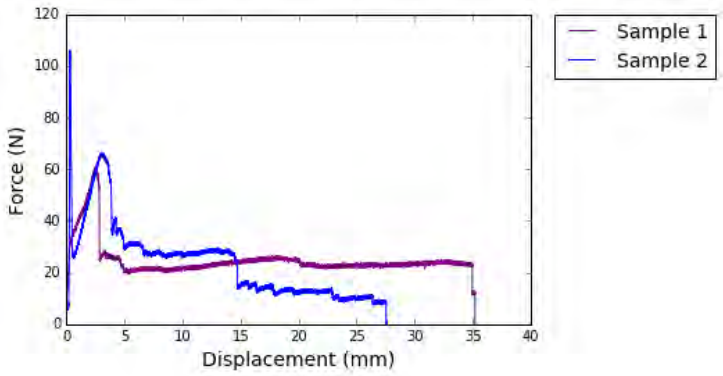

Figure 6.1: Load-displacement curves for mode I FML samples

6.2 TSA & Side View Mode I Results

A total of four (4) sub-figures are processed for two mode I FML samples as indicated in Figure 6.2. Due to ARAMIS sensitivity issues however, the TSA measurement technique was not able to accurately determine the crack length as later discussed. This therefore only provides side view calculations where each samples SERR values have been calculated approximately every 2.5mm with respect to crack length. Across the sub-figures (6.2a to 6.2c), the variation of results further indicates a compromise between the sample 1 FML interface.

Figure 6.2a provides the MBT reduction scheme of samples 1 and 2 with respect to the crack length using the side view technique. The results indicate sample 1 crack initiation (G_{Ic}) occurs at 0.1868 N/mm followed by sample 2 at 0.3016 N/mm. Furthermore, both samples indicate a continuous trend as the crack extends along the FML interface with sample 1 and 2 reaching steady state ($G_{I\infty}$) at a crack length of approximately 15mm with sample 1 at 0.1124 N/mm and sample 2 at 0.2607 N/mm.

The J-integral reduction scheme is provided in Figure 6.2b and indicates crack initiation SERR values (J_{Ic}) within 6% between each sample. Crack initiation follows the same trend in the MBT results with sample 1 resulting in the higher crack initiation SERR values at 0.00103 N/mm followed by sample 2 at 0.001099 N/mm. In addition, SERR steady state values ($J_{I\infty}$) in samples 1 and 2 resulted in 0.00538 N/mm and 0.00815 N/mm at a difference of 12% respectively. However, $J_{I\infty}$ indicates to be increasing beyond MBTs steady state crack length of 15mm further suggesting its steady state value is occurring beyond the measured values.

Figure 6.2c further provides the crack-displacement curves of the two samples following a similar trend in the previous figures. Sample 2's crack length initiates at 3.12mm with sample 1 at 2.66mm respectively. In addition at a final measured crack length of 20mm, sample 2 reaches a displacement of 13.21mm with sample 1 at 6.87mm. Figure 6.2d provides the steady state MBT and J-integral values with respect to the side view measurement technique in sample 2 indicating a a variation of approximately 0.25 N/mm between the chosen reduction schemes with $J_{I\infty}$ and $G_{I\infty}$ SERR values at 0.00815 N/mm and 0.2607 N/mm.

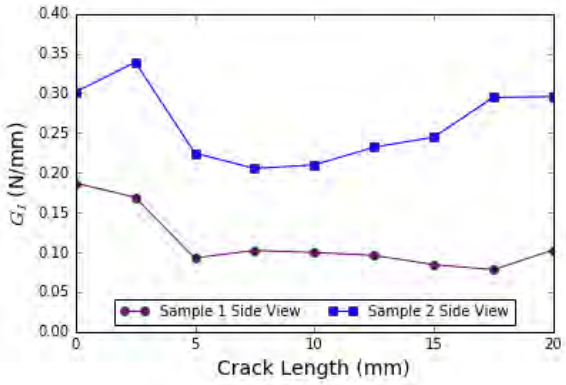

(a) Crack growth resistance curve using side view with MBT

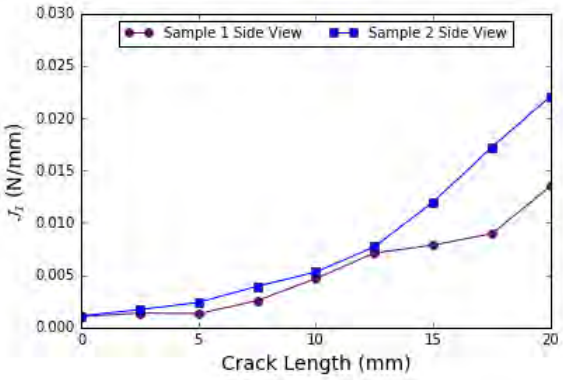

(b) Resistance curve using side view with J-integral

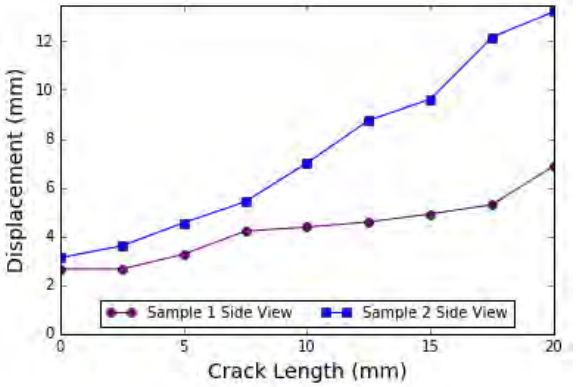

(c) Analysis of crack length in samples using side view

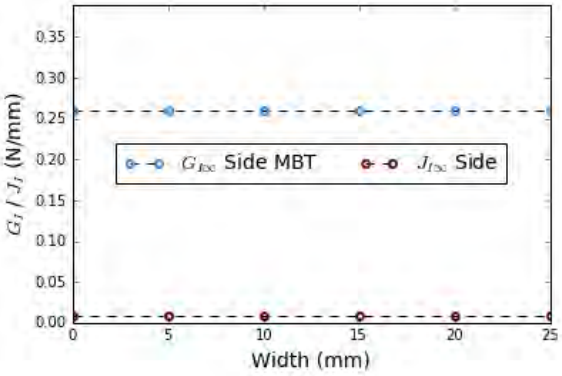

(d) Distribution of $G_{I\infty}$ and $J_{I\infty}$ along the width of Sample 2

Figure 6.2: Side view FML results under mode I loading

6.3 VCCT Results

Figure 6.3 indicates the FEM results using the VCCT method and provides SERR values at a loaded displacement of 1.3mm along each material substrate (2.6mm in total). This value corresponds to the average total deformation experienced in the two samples as provided by the load-displacement curve (Figure 6.1). The VCCT results indicates that as calculated, the mode I is dominant with a total value of G_I equal to 0.055 N/mm and G_{II} equal to 0.001 N/mm. Figure 6.3 further provides the VCCTs ability to capture the SERR values along the width caused by the onset of the triaxial stress state.

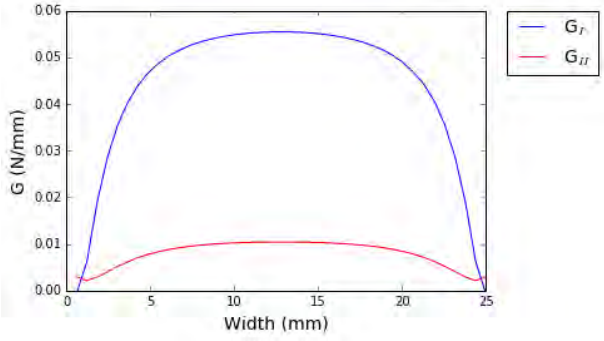

Figure 6.3: Mode I VCCT SERR values

6.4 Discussion

Mode I FML samples have been tested and analysed using the side view measurement technique in conjunction with the MBT and J-integral schemes. Their results are provided in Table 6.1. However, due to time constraints and the ARAMIS machine (TSA) instability issues, only two samples were able to be tested. Across the two samples, a variation in the results is observed raising concerns. Following the experiment, a post test inspection is conducted on both the samples surfaces to observe the FML interface. This is provided in Figure 6.4 and assists in explaining the discrepancy between the samples SERR values.

In addition, efforts were previously made in Section 2.4.2 (refer Equation 2.7) to ensure mode I fracture was occurring. This has been further confirmed through the FEM VCCT model indicating its success.

Table 6.1: Mode I side and TSA results with MBT and J-integral

	MBT				J-Integral			
	Side		TSA		Side		TSA	
	G_{Ic}	$G_{I\infty}$	G_{Ic}	$G_{I\infty}$	J_{Ic}	$J_{I\infty}$	J_{Ic}	$J_{I\infty}$
Sample 1	0.1868	0.1124	-	-	0.001035	0.00538	-	-
Sample 2	0.3016	0.2607	-	-	0.001099	0.00815	-	-

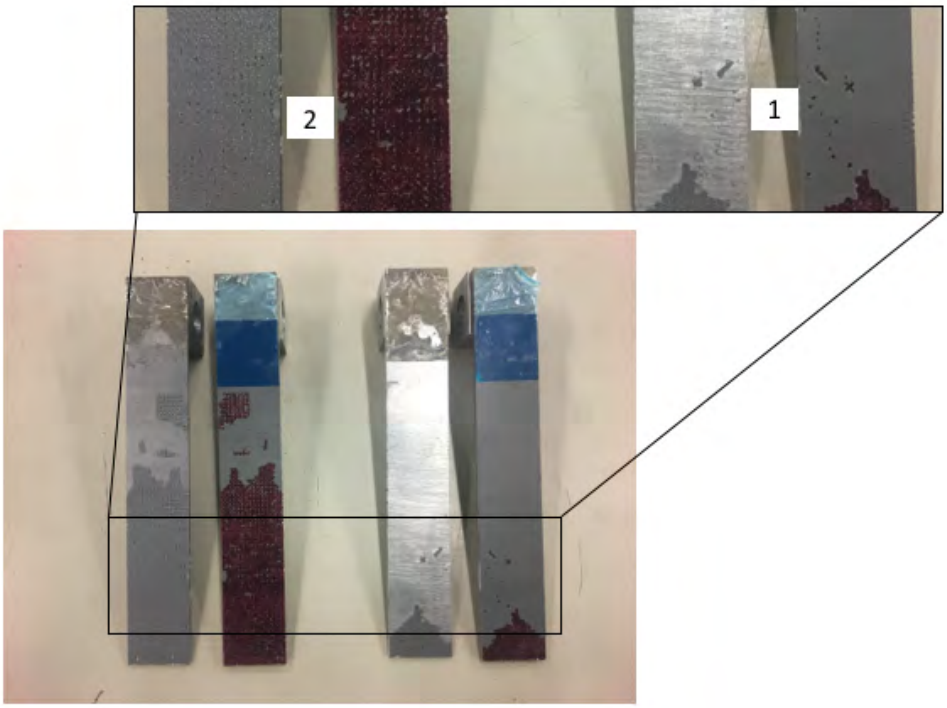

Figure 6.4: Mode I FML samples post testing surface inspection

The load-displacement curve previously provided in Figure 6.4 indicated in sample 2 the stick-slip behaviour. This is explained by the Loctite 9394 epoxy attaching itself to the high points where the twill woven GFRP fibres overlap each other. This saw-tooth type response is commonly observed across FML materials and indicates the ideal bonding case between the interface. Furthermore, this indicates discontinuous crack growth which

occurs from the fibres restricting delimination [33], thus requiring an increase in load. However, at displacements between approximately 5mm to 15mm where no saw-tooth response is observed, sample 2 exhibits a non-ideal bonding. This is further provided in the post test surface inspection where the the interface shows favourability to the GFRP surface. Furthermore, sample 1 appears to have the FML interface compromised along the majority of its length (except for at displacements of 0 to 5mm) showing minimal epoxy on the steel surface. This corresponds to a lack of a saw-tooth pattern and instead indicates stable crack growth. This is further indicated in the post test surface inspection (Figure 6.4) with the steel surface showing consistent horizontal delamination lines across the sample as the crack extends along the FML interface.

The corresponding non-ideal bonding between the displacements of 5mm to 15mm in sample 2 and through the majority of sample 1 is able to be distinguished through both the MBT and J-integral schemes. This is further provided in Figures 6.2a and 6.2b that at a crack length of 15mm and beyond, a divergence in the samples is observed. In comparison to the J-integral and MBT schemes, the J-integral resulted in lower crack initiation and steady state SERR values to the MBT scheme. However, the MBT appears to reach steady state SERR values at earlier crack lengths in comparison to the J-integral which appears to reach steady state beyond the final measured crack length. However, this may be effected due to the compromised FML interface in the samples as previously discussed. Furthermore, the J-integral scheme underestimates initiation values with the MBT scheme overestimating values in comparison to the VCCT method. The discrepancy between values is explained by how each scheme measures SERR values (refer Chapter 5).

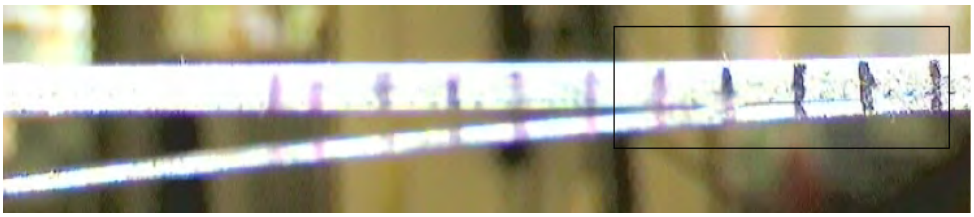

Figure 6.5: Premature side view analysis from voids along both samples edges

An inspection previously revealed voids along the edge of the sample raising concerns in the side views premature approximation of the crack length upon delamination. The side view analysis is provided in Figure 6.5. It further highlights the side view techniques lack of ability to determine the crack length relying heavily on the skills of the user. However, TSA was not able to be compared due to ARAMIS' sensitivity issues thus not being able to quantify the impact of voids along the edge may have caused. It is only from the inspection and from past literature it is known the impacts the side view has SERR values [45].

Figure 6.6 indicates the reasoning behind why the TSA measurement technique was not able to be implemented. Point displacements along the length of the sample were not able to be accurately measured. This suggests ARAMIS has experienced issues in updating the reference plane in order to calculate distances however due to TSAs recent development, a more defined explanation cannot be stated.

The concern with the FEM VCCT model is due to requiring intrinsic fracture properties (G_c) in regard to each of three modes. This is required in order to simulate crack

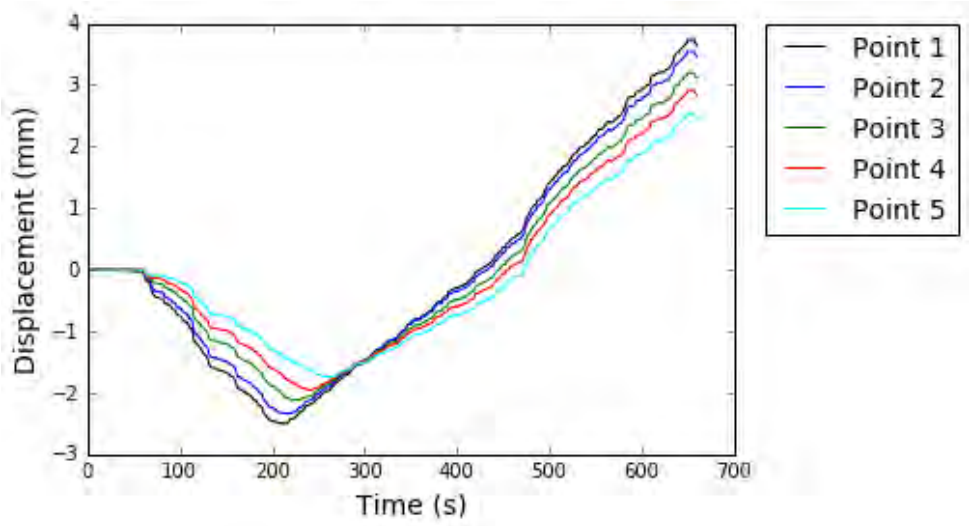

Figure 6.6: ARAMIS (TSA) instability issues

propagation and therefore, the major assumption regarding the model is that the:

displacements experienced from experimental testing is equal to the intrinsic SERR values required to initiate crack propagation.

This explains that for any increase in the displacement value input into the model, will further increase the SERR values (refer Figure 6.3). The benefit of the VCCT method presented here however is that; (1) there is confirmation that mode I loading occurs further providing success to the method outlined earlier (Equation 2.7) and (2) provide a basis of comparison to the measurement technique SERR values.

Overall, due to the time constraints, it is unable to provide additional SERR values through sample testing. However, it is expected following tests will be more suited to sample 2's trend at crack lengths from 0 to 5mm and 15 to 20mm where unstable crack growth has been identified and further asserted from the typical saw-tooth pattern response observed. Furthermore, no statement can be made regarding the TSA technique due to the instability issues.

6.5 Conclusion

Concluding the mode I FML samples analysis and discussion, numerous observations have been stated. These include:

1. The variation of the SERR values provided early in Table 6.1 can be directly related to the observed post test surface inspection and load-displacement response curve.

2. Sample 1 has resulted in a compromised interface requiring less force to extend the crack along the FML interface, thus calculating lower SERR values. Furthermore, sample 2 has a partially compromised interface.

3. Following the post test inspection on the FML sample interfaces. Both the MBT and J-integral schemes are capable of identifying between ideal and non-ideal bonding scenarios albeit at their respective magnitudes using the side view technique.

4. In comparison to the MBT and J-integral schemes; the MBT suggests it is capable of calculating steady state values at earlier crack lengths in comparison to the J-integral, which appears to reach steady state beyond the measured crack length. Furthermore, the J-integral overall calculates lower initiation and steady state SERR values across both samples.

5. The MBT scheme appears to be more suitable in calculating mode I SERR values in comparison to the VCCT model.

6. Voids along the edges of the mode I FML has effected the side view measurement technique results. Due to TSAs instability issues however, the level of degree to which it is effected it is not able to be quantified.

7. The method outlined in ensuring a mode I FML exhibits only mode I SERR values is successful with the VCCT method confirming minimal mode II influence. Furthermore, the VCCT model is suitable under its stated assumptions providing an effective method in providing a basis for SERR values.

Chapter 7

Mixed Mode FML Analysis

The mixed mode FML samples are of interest due to allowing a direct comparison to the mode I results as well as concluding whether TSA and the side view measurement technique were able to distinguish between each of the modes. Furthermore, this chapter outlines the results for the mixed mode FML samples and compares two mixed mode samples. Following the results, a discussion is provided outlining the variations of the results between each mixed mode samples.

7.1 Mixed Mode Interface Characterisation

The mixed mode FML hybrid composite is made up of 24 plies (2.496mm) of HexPly 914 S-glass and a 8mm steel panel making up a total thickness of 10.896mm once bonded together. The ADCB experiments follow the same procedure as its DCB counterpart as outlined in the initial mode I case (refer Chapter 6).

The load-displacement curves of the two samples are provided in Figure 7.1 and indicate delamination between sample 1 and 2 occur at loads of approximately 150N and 120N and displacements at approximately 2.5mm and 3.5mm respectively. Sample 2 shows a premature peak at approximately 50N and is explained by the Loctite 3421 epoxy covering the precrack when clamping the loading blocks to the samples. Consistent across both samples, a stick-slip (saw-tooth) response is observed, a common characteristic associated with bonded FMLs materials indicating ideal bonding between the GFRP and steel interface [33]. Furthermore, time constraints restricted the possibility of additional testing of mixed mode samples.

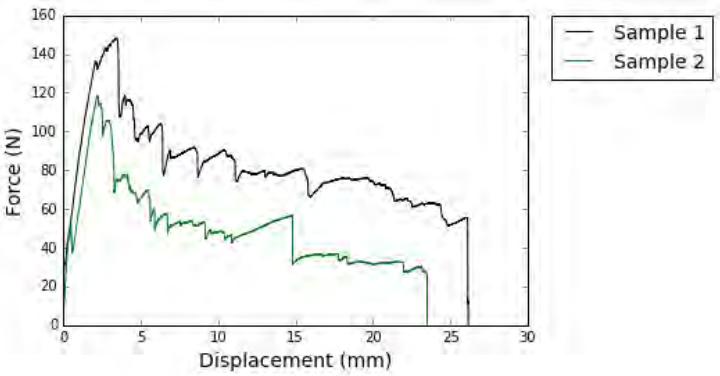

Figure 7.1: Load-displacement curves for mixed mode FML samples

7.2 TSA & Side View Mixed Mode Results

Each sample has been analysed using the TSA and side view measuring techniques used in conjunction with the MBT and J-integral methods. TSA points have been selected at the midsection of each specimen and is fitted with a fifth order polynomial with the side view analysing only the edge surface of the sample. Both samples have been measured based off approximating the crack length every 2.5mm and follows the methodology as provided in Section 4.2.2.

Figure 7.2c compares the two measuring techniques with respect to crack length and displacement experienced upon loading. The value across both the TSA and side view indicate a continuous trend as the crack extends along the FML interface increasing the displacement. Furthermore, the results indicate that TSA is able to detect crack propagation earlier at 0.008mm in sample 1 and 0.006mm in sample 2 in comparison to the side views 3.43mm and 2.19mm. Overall, TSA results in a lower displacement at a final measured crack length of 20mm with 0.006mm in sample 1 and 0.08mm in sample 2 in comparison with the side view technique at 2.19mm and 3.43mm in samples 1 and 2 respectively.

Figure 7.2a provides the TSA and side view techniques used with MBT. It is indicated across both samples that the side view estimates a higher SERR crack initiation values (G_{Ic}) in samples 1 and 2 at 0.2917 and 0.2280 N/mm in comparison with the TSAs MBT at 0.02674 and 0.0026 N/mm. Furthermore, both measurement techniques indicate steady state values at a crack lengths beyond 7.5mm. The side view samples correspond to a MBT steady state ($G_{I\infty}$) in samples 1 and 2 at 0.2729 and 0.2118 N/mm to that of TSAs at and 0.1735 and 0.09577 N/mm.

The TSA and side view measurement technique used in conjunction the J-integral is provided in Figure 7.2b. Consistent across both the TSA measurement techniques, crack initiation (J_{Ic}) occurs within both samples at approximately 0.42 and 0.66% of each other respectively. This corresponds to TSA J_{Ic} values in samples 1 and 2 at 0.00377 N/mm and 0.0024 N/mm in comparison with the side view at 0.003786 N/mm and 0.002416 N/mm respectively. Furthermore, a similar trend is observed with respect to TSA and side view techniques as the crack extends along the FML interface in calculating steady state ($J_{I\infty}$) SERR values. This corresponds to TSA $J_{I\infty}$ values at 0.05732 N/mm and 0.03250 N/mm in samples 1 and 2 in comparison to the the side view $J_{I\infty}$ values at 0.05026 N/mm and 0.05732 N/mm.

Figure 7.2d provides the SERR initiation and steady state values across the width of sample 2. A third order polynomial fit is provided across the TSA to approximate the following points not presented with a linear fit for the side view technique. The figure indicates TSAs ability to capture SERR values across the width of sample 2 using the MBT and J-integral reduction schemes. Furthermore, the results provide SERR crack initiation values (J_{Ic}) in the TSA occurring at 0.0024 N/mm before reaching the steady state value of 0.0325 N/mm. In comparison, the side view technique in sample 2 indicates initiation (G_{Ic}) and steady state ($G_{I\infty}$) SERR values at 0.002416 N/mm and 0.05732 N/mm respectively.

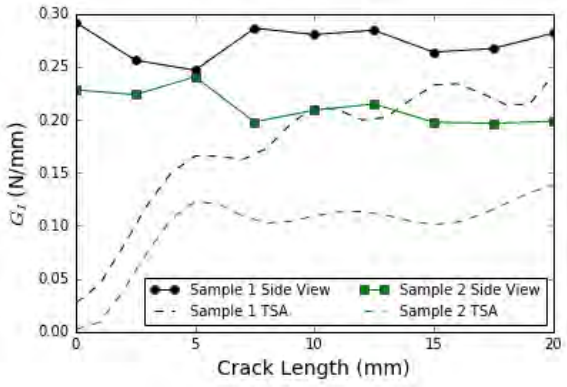

(a) Crack growth resistance curve using side view and TSA with MBT. TSA analysis on each samples midsection.

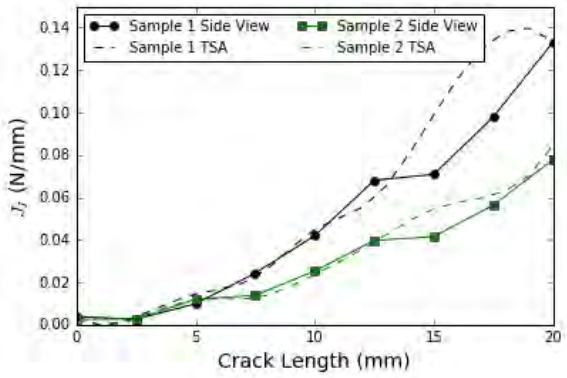

(b) Resistance curve using side view and TSA with J-integral. TSA results fitted to fifth order polynomial.

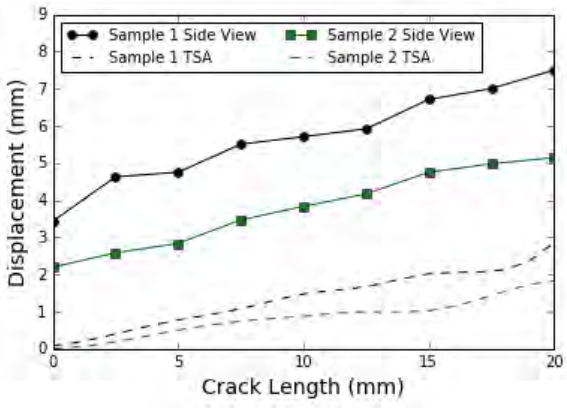

(c) Analysis of crack length in samples using side view and TSA

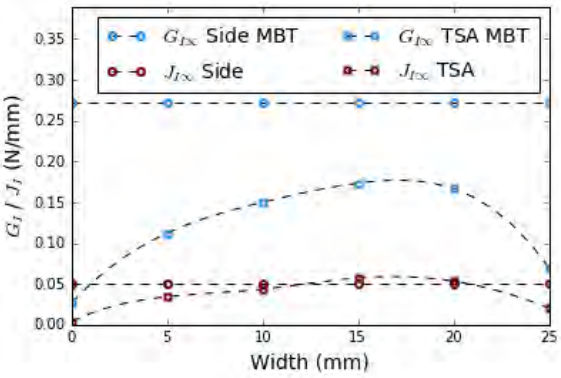

(d) Distribution of G_I along the width of Sample 2

Figure 7.2: Side view and Top Surface Analysis results under mixed mode loading

7.3 VCCT Results

The Virtual Crack Closure Technique model is provided in Figure 7.3 and provides results at an input displacement of 1.5mm input along each substrate (3mm in total). This value corresponds to the average total deflection experienced in the two samples upon delamination (refer Figure 7.1). The VCCT model indicates mode I and mode II fracture properties with their maximum values experienced at the width of the sample due to the triaxial stress state. Mode I (G_I) SERR values occur at a maximum value of 0.144 with mode II (G_{II}) at 0.09 N/mm indicating that mixed mode loading theoretically is occurring in the FML samples.

7.4 Discussion

Table 7.1 summarises the SERR values across samples 1 and 2 from applying the MBT and J-integral in conjunction with the side view and TSA measuring techniques. Due to time constraints however, only two samples were able to be tested leading to concerns in the reliability and precision of the values presented. In addition, a post test surface inspection is provided to compare the calculated SERR values to the load-displacement curves observed and assist in explaining disparities.

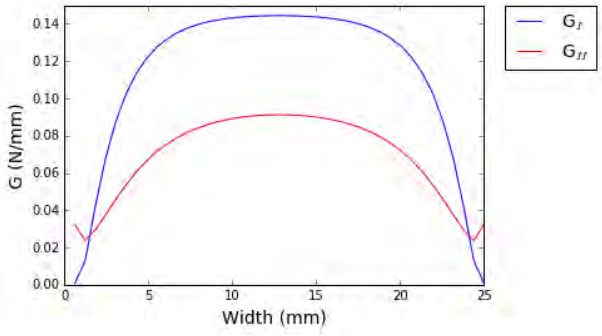

Figure 7.3: Mixed mode VCCT SERR values

Table 7.1: Mixed mode side and TSA results with MBT and J-Integral

	MBT				J-Integral			
	Side		TSA		Side		TSA	
	G_{Ic}	$G_{I\infty}$	G_{Ic}	$G_{I\infty}$	J_{Ic}	$J_{I\infty}$	J_{Ic}	$J_{I\infty}$
Sample 1	0.2917	0.2729	0.02674	0.17350	0.003786	0.05026	0.003770	0.05732
Sample 2	0.2280	0.2118	0.00260	0.09577	0.002416	0.05732	0.002400	0.03250

The post test surface inspection of both the samples indicated that from interfaces rough exterior, a stick-slip response has occurred. This confirms that ideal bonding has occurred across both samples. In comparison to the load-displacement curves previously indicated in Figure 7.1, sample 2 is observed to delaminate prematurely and may be due to a combination of; (1) uncertainty surrounding misalignments of the loading blocks which may have led to mode III loading or (2) corrosion along the precrack or edges. This is effect would lead to a decrease in the calculated energy release rates. In addition, sample 1 appears to have an increased stiffness response as indicated in Figure 7.1 at crack lengths between 0 to 3mm (increased gradient) which may further provide the samples variance in SERR values. Observed in Figure 7.1, both samples can be seen to increase in period (increase of saw tooth pattern) beyond displacement values of 10mm and further suggests; (1) the samples begin to exhibit mode II loading or (2) the increased stiffness within each substrate has magnified the saw-tooth pattern as previously observed in mode I samples. However, mode II loading was observed in the post test figures including; Figure 7.4 indicating the surface inspection of the samples and Figure 7.5, indicating in sample 2 that the interface begins to delaminate along both material substrates. The load-displacement figure as well as the post test surface inspection assists in explaining the variation in the SERR values in the samples.

Figure 7.2a and 7.2b indicate the MBT and J-integral schemes using both the TSA and side view measurement techniques. The figures indicate that as a result of sample 2's premature failure, or rather because of sample 1's increased stiffness response, the MBT and J-integral calculate lower SERR values. This can be seen more clearly in Figure 7.2c indicating lower crack initiation with respect to displacement. Using the MBT scheme, both the TSA and side view technique indicate steady state SERR values beyond crack lengths of 10mm. However, the TSA and side view with the J-integral scheme show a continuous increase J_I values raising concern to the steady state ($J_{I\infty}$) values calculated.

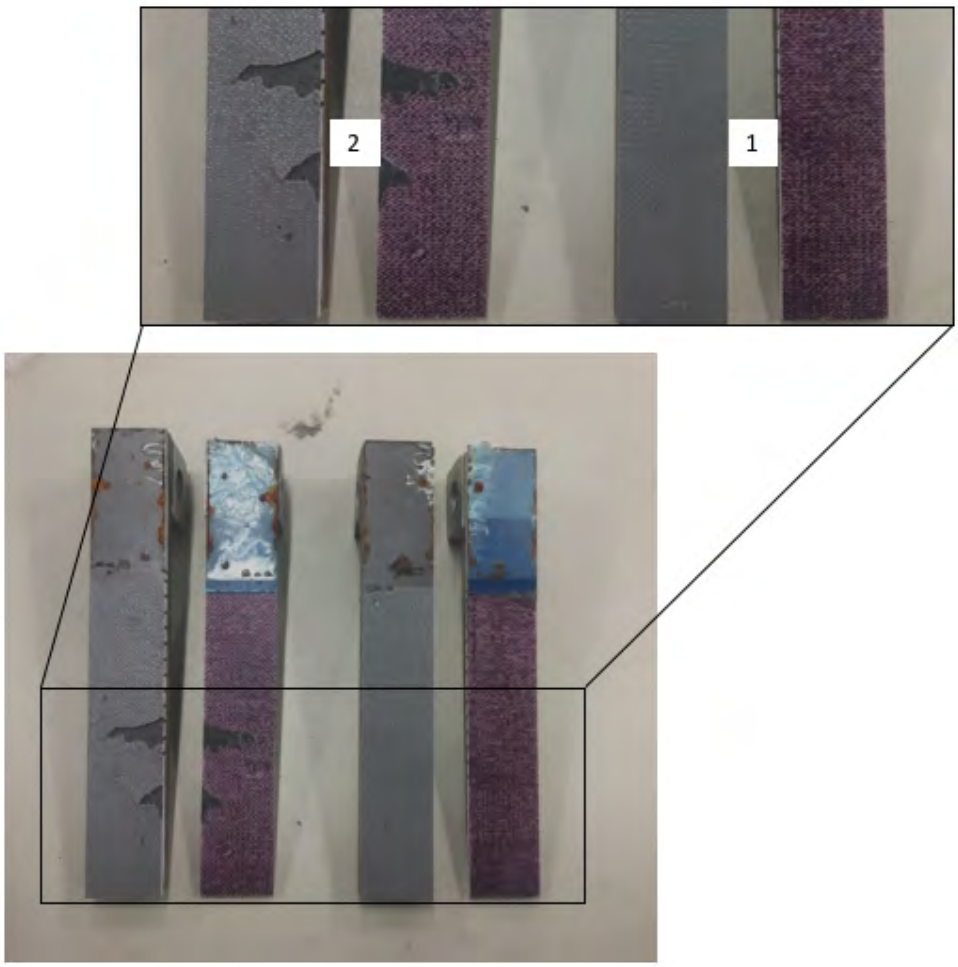

Figure 7.4: Mixed mode FML samples post testing surface inspection

Interestingly, between the two samples at a crack length of 5mm, particularly with the side view technique using the MBT scheme, the samples SERR values begin to diverge from each other. TSA on the other hand was able to distinguish a disparity before a crack length of 5mm between the two samples using MBT however not using the J-integral. The crack-displacement curve in Figure 7.2c indicates no clear signs of why this occurs however, it is suggested that it is due to a rapid decrease in corresponding load as indicated in the load-displacement curves (Figure 7.1). In addition, using the MBT scheme (Figure 7.2a) at crack lengths below 5mm indicate there is large discrepancy between the TSA and side view method in regard to G_{Ic} values. Furthermore, it is observed that TSA shows a constant increase in SERR values to the side views somewhat constant plateau. This however, may be explained by the J-integrals omission to not calculate SERR values based directly from displacement readings and instead relies on force and crack length values (refer Chapter 5). Furthermore, each technique/scheme between the two samples across the MBT and J-integral show consistent trends for an increase in crack length indicating success in the ad-hoc method of manually measuring points as well as syncing the measurement techniques and INSTRON machine to a local time frame.

Figure 7.2d highlights TSAs ability to approximate SERR values across the samples width, a feat the conventional side view is not able to accomplish. It further points out TSAs benefit in conjunction with the J-integral showing the width at approximately 22mm values close to the steady state values. The major concern in pointing out this

accuracy however is that the J-integral in Figure 7.2b indicates calculations of J_I further increasing beyond the final measured crack length at 20mm. This would therefore require further testing before any defined statement as it is believed measuring beyond a crack length of 20mm would further increase the steady state SERR values. Furthermore, TSA SERR values across the width are successful to a degree using both the J-integral and MBT method. This however comes prematurely due to only having tested two samples and when considering the large magnitude between the values, requires further testing.

From the microscopy images it was observed that mixed mode was not effected by voids located along the edges from water jet cutting. However, from there only being two samples tested, it is further required to assess whether any effect of premature crack lengths were approximated using the side view.

Figure 7.5: Mixed mode sample 2 exhibiting shear loading along the FML interface

The major concern with the FEM modelling is under its assumption already previously indicated as part of the mode I analysis (refer Chapter 6). Furthermore, a literature search indicated that no such experimental testing has existed for this specific hybrid composite. This therefore provides a simplistic approach in confirming the sample will be highly influenced by mixed mode (i.e mode II) loading prior to testing as well as a rough estimate to compare values too. In comparing the VCCT model G_I to the distribution of G_I using the MBT, values are approximately equal however to further assert this statement, a simulated crack model is required. A comparison between the mixed mode TSA SERR values in comparison to the VCCT model is further developed in Section 8.6.

7.5 Conclusion

From conducting the mixed mode experiments on two samples, the results suggest:

1. Ideal bonding has occurred in the mixed mode FML samples due to observing a typical saw-tooth pattern from the load-displacement curves. Furthermore, premature crack initiation in one of the samples may be reasoned to contributions of surface corrosion and mode III loading.

2. In regard to the MBT method, the side view results in greater values in comparison to the TSA. At crack lengths greater than 10mm, both the side view and TSA measuring techniques appear to reach steady state. However in regard to the J-integral, both the side view and TSA measurement techniques show a continuous

increase beyond the final measured crack length value suggesting concerns to the steady state values presented.

3. Both the TSA and side view techniques using the MBT and J-integral schemes show consistent trends between the two samples tested indicating their success.

4. The VCCT model provides a simple method to ensure mixed mode is occurring. This further iterates that mode II is present in the mixed mode FML samples before experimental testing commenced.

5. The post test surface inspection as well as the load-displacement curves provide simplicity in understanding the SERR values and assists in explaining the disparity in results.

6. The MBT scheme with TSA has approximated steady state SERR values approximately equal to the VCCT model however, further testing of mixed mode samples is required before any distinct conclusions can be stated due to only having tested two samples.

Chapter 8

Mode I and Mixed Mode Results Comparison

This chapter provides the direct comparison between the mode I and mixed mode samples. It further determines if TSA and the side view measuring techniques were capable of distinguishing between mode I and mixed mode loading. Unlike the previous chapters which focused on the analysis between mode I *or* mixed mode samples, this chapter provides the direct comparison.

Figures have been placed side-by-side as well as being plotted on the same y-axis scale to provide simplicity in observing the results. Furthermore this chapter discusses and concludes whether mixed mode was capable of being distinguished in FMLs using side view and TSA in conjunction with the MBT and J-integral reduction schemes.

8.1 Load-Displacement Results

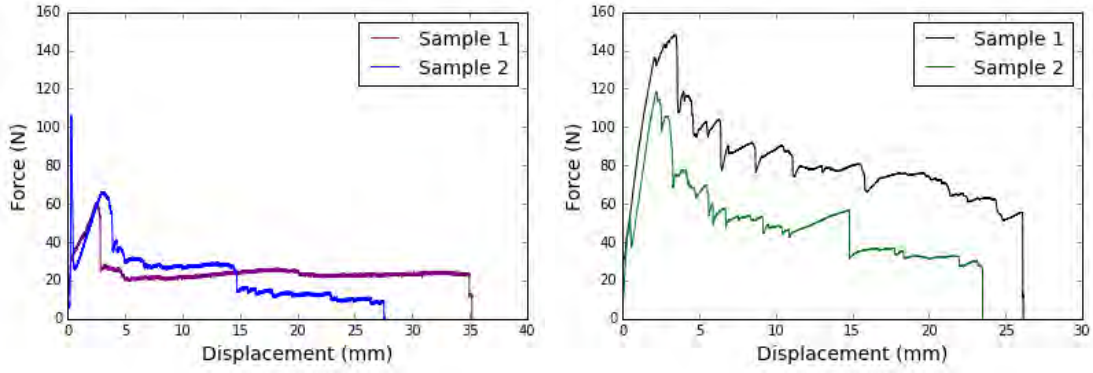

(a) Mode I (b) Mixed mode

Figure 8.1: Comparison of mode I and mixed mode load-displacement curves

Figure 8.1 provides the mode I (Figure 8.1a) and mixed mode (Figure 8.1b) FML samples throughout the INSTRON testing. They indicate; (1) the mixed mode FML samples increase in load in order to initiate crack propagation along its interface at 150 and 120N to mode I's 60N as well as (2) the increased stiffness of the mixed mode samples. In addition, mode I's sample 1 has previously been discussed to provide a non-ideal bonding scenario which has led to mode I's sample 2 to be used for comparison. Furthermore, crack initiation of all the samples occurs at displacements between approximately 2 to 4mm.

8.2 TSA Results

TSA was not capable of capturing mode I samples due to instability issues. Figure 8.2 provides the TSA points displacement with mixed mode (Figure 8.2b) in comparison to mode I (Figure 8.2a). The figures further indicate why it was not able to be calculated as it is approximating negative and inconsistent point displacement values as well as crack length values. This further affects the MBT and J-integral results when attempting to compare the TSA and side view measurement techniques.

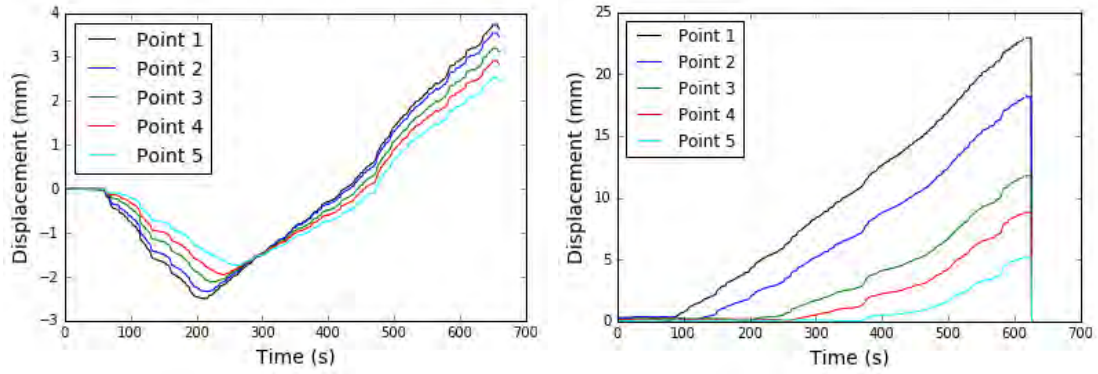

(a) TSA mode I

(b) TSA mixed mode

Figure 8.2: Comparison of Mode I and mixed mode TSA point displacements

8.3 Crack-Displacement Results

The crack-displacement plots are shown in Figure 8.3 and it provides a clear distinction between the mixed mode samples and mode I's sample 2. The mixed mode displacement values at a final measured crack length are 7.5mm and 5.14mm in comparison to mode I's sample 2 of 13.21mm. It is also observes the mixed mode samples slower crack propagation resulting from the samples increased stiffness.

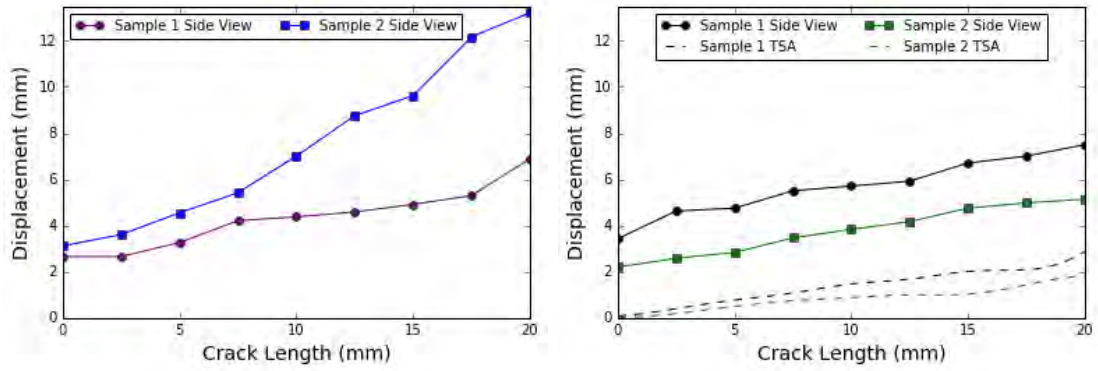

(a) Mode I

(b) Mixed mode

Figure 8.3: Comparison of mode I and mixed mode crack length-extension

8.4 MBT & J-Integral with TSA and Side View Results

Figures 8.4 and 8.5 provide the MBT and J-integral values where a distinct comparison can be made between the side view methods. As previously discussed however, a direct comparison for TSA cannot be made due to ARAMIS' instability issues. The results further indicate (Figures 8.4 and 8.5) MBTs difficulty in observing mixed mode loading with all three (3) ideal bonded samples calculating crack initiation G_{Ic} and steady state SERR $G_{I\infty}$ values within 0.06 N/mm of each other. Due to ideal bonding cases between the mixed mode loading samples, crack initiation and steady state SERR values are more easily defined to values within; 0.22 N/mm $\leq G_{Ic} \leq$ 0.30 N/mm and 0.21 N/mm $\leq G_{I\infty}$ $\leq$ 0.28 N/mm however with mode I, only one sample (sample 2) can be stated at and therefore has no basis for comparison.

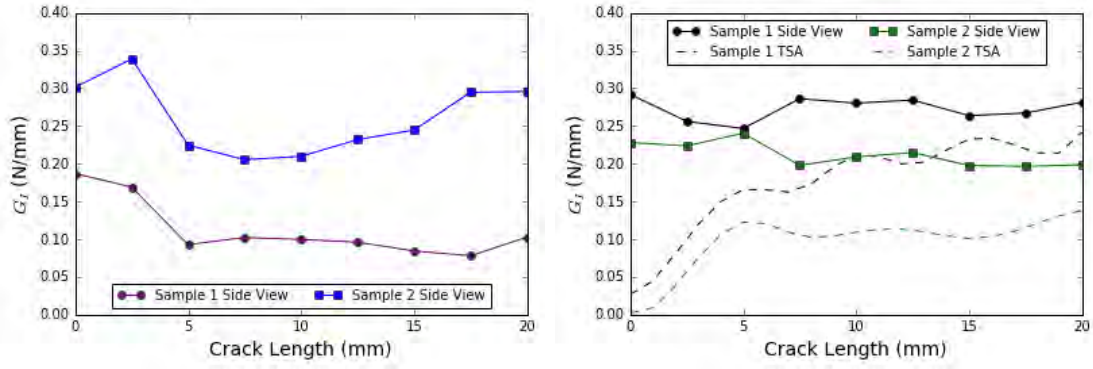

(a) Mode I (b) Mixed mode

Figure 8.4: Comparison of mode I and mixed mode MBT values

Observed in Figure 8.5, the side view technique using the J-integral shows a clear distinction in SERR values. However, consistent across both mode I and mixed mode samples, steady state SERR values raise concern as a continuous increase in J_I is observed suggesting a *true* steady state value occurs beyond the final measured crack length of 20mm. The values indicate across the mixed mode samples using side view that; 0.002416 N/mm $\leq J_{Ic} \leq$ 0.00377 N/mm and 0.05026 N/mm $\leq J_{I\infty} \leq$ 0.057 N/mm. Mode I, as previously indicated only has one test for comparison and therefore cannot provide a basis.

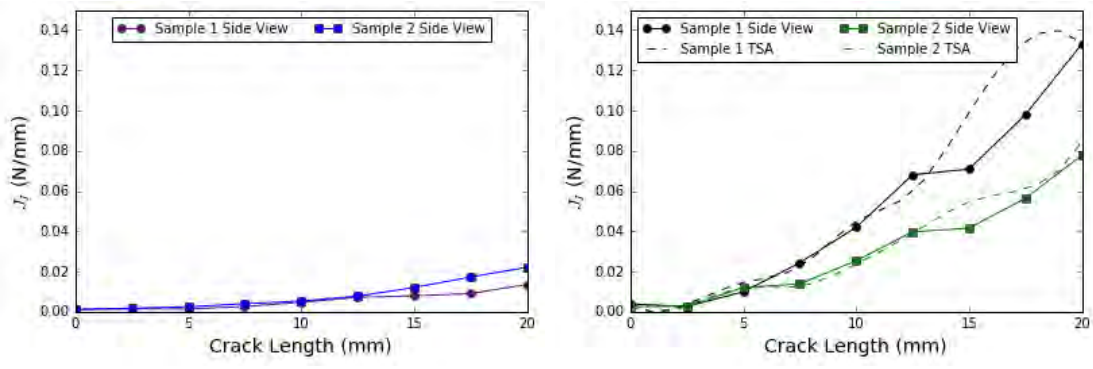

(a) Mode I (b) Mixed mode

Figure 8.5: Comparison mode I and mixed mode J-integral values

The steady states of both the mixed mode and mode I's sample 2 have been plotted. The mixed mode results indicate TSAs ability to calculate SERR values across the width of the sample, a feat the conventional side view technique is unable to accomplish. Furthermore, in comparing the values it reiterates the side view technique with the MBT schemes difficulty in distinguishing between mode I ($G_{I\infty}$) at 0.2607 N/mm in comparison to the mixed mode ($G_{I\infty}$) at 0.2729 N/mm. Figure 8.6 further provides the J-integrals ability to distinguish between mode I and mixed mode loading with mode I ($J_{I\infty}$) at 0.00815 N/mm and mixed mode ($J_{I\infty}$) at 0.05026 N/mm.

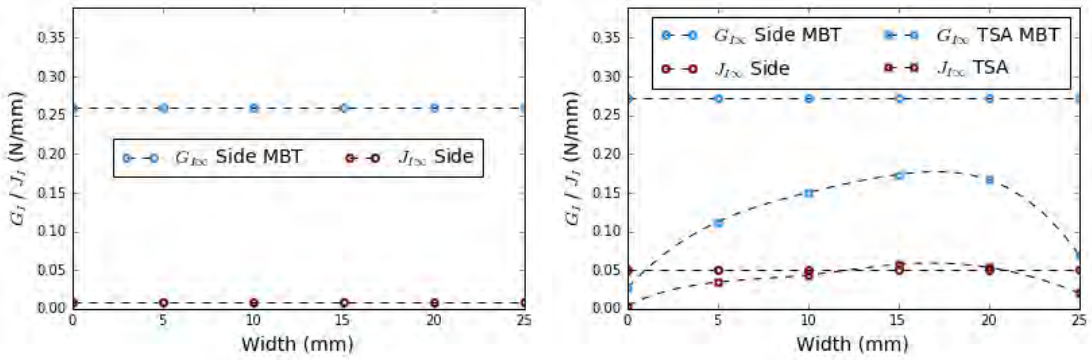

(a) Mode 1 (b) Mixed mode

Figure 8.6: Comparison of steady state mode I (sample 2) and mixed mode (sample 1) SERR values across MBT and J-integral values using side view and TSA

8.5 VCCT Results

The FEM VCCT model results for mode I and mixed mode are provided in Figure 8.7. The model provides that mixed mode undergoes a total mode II (G_{II}) SERR value of 0.09 N/mm, indicating an increase of 90% to mode I's (G_{II}) of 0.001 N/mm. Furthermore with the mode I sample inhibiting small mode II SERR values, the method previously indicated is successful (refer Equation 2.7).

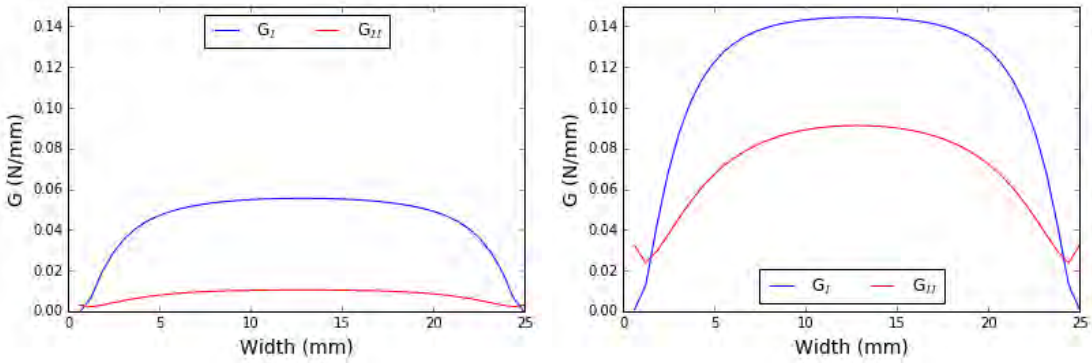

(a) Mode I (b) Mixed mode

Figure 8.7: Comparison of mode I and mixed mode FEM VCCT model

8.6 Discussion

The mixed mode and mode I samples have been compared side-by-side in order to identify if TSA and the side view measurement technique are able to distinguish between mode I and mixed mode loading. However, unlike the preceding discussions which focused on the direct comparison *between* samples and their results, there exists large uncertainties with concluding on such statements in comparison to mode I and mixed mode samples. This is due to:

1. TSA was not able to be analysed using the mode I samples and therefore cannot be compared between the two sets of samples manufactured.

2. Mode I's sample 1 has a compromised interface due to non-ideal bonding. This therefore only provides one sample (sample 2) to compare side view results.

3. Mode I was further inspected and indicated voids along the edges was visible (Figure 3.14) along both samples. This reveals further inconsistency for any measurable comparison to be made as it was not observed on the mixed mode samples.

It is therefore only possible to provide statements which appear to be of interest or indicate a high probability of being able to be confirmed upon further testing. In addition, the results are discussed nonetheless however uncertainties are pointed out where applicable.

The mixed mode samples, due to having thicker steel and GFRP substrates show increased loads at crack initiation as indicated in Figures 8.1 and 8.3. The figures further indicate that due to the mixed modes thicker substrates, an increased stiffness is observed. In addition, the crack-displacement curves provided mode I 's sample 1 inconsistent results showing values approximately equal to the mixed mode case. When comparing the load-displacement curves (Figure 8.1, there is a clear variance to the typical saw-tooth pattern exhibited in the FML samples. Due to the lack of samples tested however, this may be due to; (1) the influence of mode II loading upon inspecting the surface of the sample (refer Figure 7.4) or (2) a proportional saw-tooth pattern to mode I's sample 2 but magnified due to the mixed mode samples increased stiffness.

The MBT scheme used with side view techniques has difficulties in distinguishing between mixed mode and mode I SERR values at initiation (G_{Ic}). This is more easily identified in Figure 8.4 with various calculated values for where crack propagation initiates. In regard to the MBT side view however, there is reason to suggest the steady state SERR ($G_{I\infty}$) values are distinguishable beyond crack lengths of 7.5mm in the mixed mode samples and approximately 5mm in mode I's sample 2. However the major concern in this statement is that the mode I samples indicate non-ideal bonding between crack lengths from 5mm to 15mm as previously indicated (refer Chapter 6.4) and furthermore, voids along the edge may further be calculating inconsistent SERR values. Therefore, in order to further quantify this claim, additional testing is required regarding both sets of samples. In addition, the TSA using MBT shows a consistent trend across the mixed mode with consistent steady state values at crack lengths beyond 5mm but no comparison can be made to mode I samples. It is likely that TSA in mode I would display similar trends to its mixed mode counterpart to lower $G_{I\infty}$ values with the side view measurement technique however, no quantified justification can be made. However, this is provided on the assumption that a distinction is observed between the side view MBT steady state

SERR values.

The J-integral using the side view technique suggests its capable of distinguishing between both sets of samples however arrives at similar conclusions to the MBT figures that; (1) abnormally low values are observed for mode I samples due to voids along the edge calculating premature SERR values or (2) the mixed mode samples rapidly increase due to their increased stiffness substrates. Nonetheless, the side view technique across both the mode I and mixed mode samples using the J-integral indicate the same trend providing partial success. This can be further related to TSAs success due to the strong correlation in the mixed mode results thus it is assumed a similar trend would have been observed in the mode I samples however again, requires additional testing across both sets of samples.

The major benefit of plotting the SERR values along the width of the mixed mode samples indicates TSAs ability to produce a similar trend to the VCCT models (Figures 8.6 and 8.7b). It further indicates TSA is able to distinguish between mixed mode loading using the MBT scheme however mode I cannot be compared for comparison. This however is promising as the mixed mode TSA technique using the MBT scheme is in close proximity to the VCCT models mode I (G_I) SERR values. This is indicated further in Figure 8.8. Identified in the comparison, the results indicate increased SERR values on one width of the sample. This may be due to twisting of the GFRP top surface due to misalignments in the loading blocks however further testing is required to confirm or reject this statement. However, this requires additional testing to further confirm this statement.

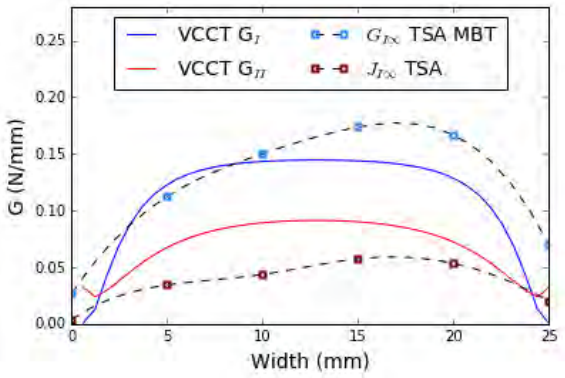

Figure 8.8: TSA mixed mode and VCCT model comparison

8.7 Conclusion

Comparisons were made between mode I and mixed mode samples within reason. Furthermore, the results revealed that TSA cannot be directly compared between the sets of the samples due to ARAMIS' instability issues in the mode I samples. A direct comparison regarding the side view technique across all the samples is limited due to mode I's non-ideal bonding scenario leaving only one sample to compare. Furthermore, mode I observed voids along the samples edges suggesting inconsistent SERR values. This has led to providing statements of interest with a high likelihood of being confirmed upon testing. The comparison has suggested that:

1. Within the side view techniques using the MBT scheme, it was not possible to distinguish between mixed mode and mode I loading at crack initiation values.

However, it is reasoned that upon further testing the steady state SERR values using the side view will be successful due to the trends observed. Furthermore, the TSA technique shows a clear indication between mode I and mixed mode loading but no comment can be made due to mode I's TSA instabilities. It is suggested that TSA would be successful upon further testing based on the conclusion of the side view MBT values.

2. The J-integral provides a clear distinction between mode I and mixed mode samples using the side view method, which is further supported with a strong correlation with TSA values. This allows partial success across the TSA and side view techniques used with the J-integral however, requires further testing for further confirmation to assert this claim.

3. The mixed mode VCCT model in comparison with TSA used with MBT provided the same trend with across the width indicating partial success in TSA to match the theoretical model. However, as no mode I TSA MBT values exist for comparison, can only be concluded as a partial success.

Chapter 9

Conclusion

Fibre Metal Laminates (FMLs) consist of thin layered composite/metal alloy sheets. Across the military, bio-medical and particularly aerospace industries. They offer advantageous mechanical properties including; increased impact tolerance, fatigue resistance and a modulus of elasticity albeit at lower densities in comparison to each included material constituent. It is from their ability to supersede conventional materials which has led to their exponential development over the past 70 years and more substantially in the last twenty years. The major issue in comparison to their benefits however is also stems from inhibiting the failures of each material constituents as well as particularly at the interface by delamination. However, assessing the failure at the interface is difficult and requires experimental procedures and advanced measurement techniques. This has led to the development of the Top Surface Analysis technique which has the known abilities to supersede the conventional side view technique.

This Thesis comprised of setting out two main objectives; (1) to produce a manufacturing procedure and a measurement technique method to specify mixed mode Strain Energy Release Rate (SERR) values and (2) to correlate data between the Top Surface Analysis (TSA) and side view measurement techniques in order to distinguish between mode I and mixed mode samples. In order to achieve these goals, past literature was researched across a variety of topics. Of which included; fracture mechanics, the TSA and side view measurement techniques, experimental testing procedures, FMLs and Finite Element Methods (FEM). This led to developing two sets of samples comprised of an FML made up of Glass Fibre Reinforced Polymer (GFRP) and steel sheets.

Research found that the GFRP-steel FML presented is rare with no literature being able to be compared. This led to research regarding other FML structures to relate their expected traits as well as identify areas of concern in their development. The major observed characteristic associated with FML materials is in their ability to prematurely delaminate along the interface, brought on by the onset of stress concentrations at the free edges as well as from non-ideal bonding. In carrying out a delamination process along the FML interface, two measuring techniques were implemented; the TSA and side view which focus on approximating the delamination (crack) length from the top and side surfaces respectively. To simulate delamination, a Double Cantilever Beam (DCB) and Asymmetric Double Cantilever Beam (ADCB) test procedure was carried out. A Finite Element Mode (FEM) labelled the Virtual Crack Closure Technique (VCCT) further provided benefits in providing a comparison between theoretical and experimental results.

Both the mixed mode and mode I samples were manufactured where the GFRP was

made up of HexPly 914 S-glass twill weave bonded to A366 steel. To ensure mode I SERR values, 21 plies of GFRP (2.184mm) was bonded to 1mm of steel with mixed mode being manufactured to 24 plies of GFRP (2.496mm) to 8mm of steel. Following the manufacturing procedure, a microscopy assessment and general inspection of the samples was conducted. The findings concluded non-ideal bonding partially between the mode I samples however not in the mixed mode samples.

The mode I samples were carried out using the Double Cantilever Beam (DCB) procedure. Provided before the testing however, an inspection by microscopy and observations revealed voids along the edge of the sample. Upon testing, one of the two samples was discovered to have a non-ideal bonding between the GFRP and steel thus compromising the interface with lower overall fracture values observed. In addition, there was success in the side view techniques ability to distinguish between ideal and non-ideal bonding as well as stable and unstable crack growth. The Modified Beam Theory (MBT) and J-integral further indicated different fracture values in comparison to each other. TSA however was not able to be compared due to TSAs instability issues.

The mixed mode samples were further carried out using a modification of the DCB procedure, labelled the Asymmetric Double Cantilever Beam (ADCB) procedure. From the load-displacement curves, ideal bonding has occurred across both the samples indicating a typical saw-tooth pattern associated with FML samples. Furthermore, the load-displacement response differed in comparison to the mode I samples and suggested; (1) the influence of mode II loading or (2) a proportional saw-tooth pattern as observed in mode I however magnified due to the mixed modes increase in stiffness properties. The results further provided that both the TSA and side view measurement techniques show consistency in identifying trends between the two samples tested, indicating their success. The VCCT further confirmed that mixed mode occurred.

A comparison between the mixed mode and mode I samples indicated a majority of uncertainties which has led to observing trends rather than stating quantifiable values. The results further indicated that at crack initiation, the side view using the MBT scheme is not able to distinguish between the two sets of samples however at steady state, it is likely that a differentiation will be observed upon further testing. Furthermore, the TSA and side view techniques shows a clear distinction at both crack initiation and steady state values between the samples tested using the J-integral indicating partial success however cannot be completely stated due to TSAs lack of results in mode I samples. The mixed mode samples in comparison with the VCCT model provided the same trend across the width of the samples further asserting its benefits in comparison to the conventional side view method.

Overall, the work provided in this project presented the manufacturing set up, testing procedures and measurement techniques associated with Fibre Metal Laminate analysis. The project further experienced first-hand the liability of non-ideal bonding between the FML interface resulting in premature delamination thus providing considerably lower fracture properties to the ideal bonding case. Overall, there is partial success in identifying between mixed mode and mode I samples using both measurement techniques and reduction schemes however, statements and conclusions are limited due to the total number of samples tested and thus requires further work.

Chapter 10

Recommendations

The following recommendations are provided in terms of the chapters presented throughout this Thesis project. It is strongly suggested to consider further work into:

Chapter 2 - Literature Review:

- A Mixed Mode Bending (MMB) test procedure was discussed. It should be further assessed to determine whether the TSA measurement technique is able to be successful as various authors have raised additional benefits to the DCB and ADCB test procedures provided as part of this thesis.
- A FEM method labelled the Virtual Crack Closure Technique (VCCT) was modelled to provide preliminary results however was unable to provide crack simulation properties due to requiring intrinsic SERR values. Therefore, it is further suggested to consider the effective means to calculate these intrinsic properties from further testing of the FML presented here or to model an already developed FML, such as GLARE and assess the results and identify whether it is possible to observe a typical saw-tooth response.

Chapter 3 - Fibre Metal Laminate Manufacturing:

- The microscopy images identified that due to not sandblasting the steel panels, the interface was compromised and resulted in non-ideal bonding between some samples. If available and further testing permits, sand blasting is encouraged to mitigate any uncertainties when analysing results.
- Voids along the edges were present in the mode I FML samples due to their overall thin thickness'. It is suggested that alternative means be developed to mitigate this issue as it has further revealed an impact on the results.

Chapter 4 - ARAMIS (TSA) & Side View Setup:

- Further understanding is required regarding ARAMIS' coding manual. This will further limit unnecessary manual labour which has been carried out as well as provide The University of Queensland with the advanced means to speed the process of providing results for newly developed FMLs.
- Sync the side view and TSA measurement techniques to the INSTRON machine. In doing so, no additional steps will be required further bypassing the necessity of syncing each measurement technique and machine to a local time frame.

Chapters 6, 7 and 8 - Results of Mode I, Mixed Mode and the Comparison:

- Apparent across both the mode I and mixed mode samples, additional testing on samples is required in order to further conclude and correlate trends across the MBT and J-integral using the TSA and side view techniques. This will allow for quantifiable statements and further confirm or reject the statements presented here.
- Specifically regarding mode I, to test additional samples using TSA such that any quantifiable comparison can be made.

Bibliography

[1] Astm orginisation. https://www.astm.org/.

[2] Qep 75 x 1.6mm v notch adhesive floor spreader. https://compareclub.com.au/groceries/qep-75-x-1-6mm-v-notch-adhesive-floor-spreader-182414.

[3] Mylar heat resistant tape. https://www.dhgate.com/product/mylar-heat-resistant-high-temperature-insulation/387750107.html, 2018.

[4] Teflon tape information. https://www.windsorfoodmachinery.com/stock/50mm-teflon-tape-4212, 2018.

[5] AERO4300. Aerospace composites manufacturing and design. AERO4300 Workshop Composite Manufacturing: Hand Lay-up.PDF.

[6] Richmond Aerovac. Vacpak a6200 etfe/fluropolymer release film technical data. 2018.

[7] T. L Anderson and T. L. (Ted L.) Anderson. *Fracture mechanics : fundamentals and applications / T.L. Anderson.* Taylor & Francis, Boca Raton, FL, 3rd ed.. edition, 2005. ISBN 0849316561.

[8] Konstantinos N. Anyfantis and Nicholas G. Tsouvalis. Experimental and numerical investigation of mode ii fracture in fibrous reinforced composites. *Journal of Reinforced Plastics and Composites*, 30(6):473–487, 2011. doi: 10.1177/0731684410397682. URL `https://doi.org/10.1177/0731684410397682`.

[9] CAE Associates. Virtual crack closure technique (vcct) in ansys. https://caeai.com/resources/virtual-crack-closure-technique-vcct-ansys, 2011.

[10] CAE Associates. Ansys cohesive zone modeling. https://caeai.com/resources/ansys-cohesive-zone-modeling, 2011.

[11] Surfblack Australia. Acetone material data sheet. 265 Whitehall Street , Yarraville VIC 3013, Australia.

[12] A. A. (Alan A.) Baker and Murray L. Scott. *Composite materials for aircraft structures / [edited by] Alan A. Baker, Murray L. Scott.* AIAA education series. American Institute of Aeronautics and Astronautics, Inc., Reston, VA, third edition.. edition, 2016. ISBN 9781624103261.

[13] Stefano Bennati and Paolo S. Valvo. An experimental compliance calibration strategy for mixed-mode bending tests. *Procedia Materials Science*, 3:1988 – 1993, 2014. ISSN 2211-8128. doi: https://doi.org/10.1016/j.mspro.2014.06.320. URL http://www.sciencedirect.com/science/article/pii/S2211812814003216. 20th European Conference on Fracture.

[14] Stefano Bennati, Massimiliano Colleluori, Domenico Corigliano, and Paolo S. Valvo. An enhanced beam-theory model of the asymmetric double cantilever beam (adcb) test for composite laminates. *Composites Science and Technology*, 69(11):1735 – 1745, 2009. ISSN 0266-3538. doi: https://doi.org/10.1016/j.compscitech.2009.01.019. URL http://www.sciencedirect.com/science/article/pii/S0266353809000244. Experimental Techniques and Design in Composite Materials (ETDCM8) with Regular Papers.

[15] Michel Biron. 5 - thermoplastic processing. In Michel Biron, editor, *Thermoplastics and Thermoplastic Composites (Second Edition)*, Plastics Design Library, pages 715 – 768. William Andrew Publishing, second edition edition, 2013. ISBN 978-1-4557-7898-0. doi: https://doi.org/10.1016/B978-1-4557-7898-0.00005-6. URL https://www.sciencedirect.com/science/article/pii/B9781455778980000056.

[16] Daniel Blackwood, A W. C. Chua, K H. W. Seah, R Thampuran, and Hin Teoh. Corrosion behaviour of porous titanium-graphite composites designed for surgical implants. *Unknown*, 42:481–503, 03 2000.

[17] B. Blaysat, J.P.M. Hoefnagels, G. Lubineau, M. Alfano, and M.G.D. Geers. Interface debonding characterization by image correlation integrated with double cantilever beam kinematics. *International Journal of Solids and Structures*, 55 (Supplement C):79 – 91, 2015. ISSN 0020-7683. doi: https://doi.org/10.1016/j.ijsolstr.2014.06.012. URL http://www.sciencedirect.com/science/article/pii/S0020768314002443. Special Issue Computational and Experimental Mechanics of Advanced Materials A workshop held at King Abdullah University of Science and Technology Jeddah, Kingdom of Saudi Arabia July 1-3, 2013.

[18] F.Y.C. Boey and S.W. Lye. Void reduction in autoclave processing of thermoset composites: Part 1: High pressure effects on void reduction. *Composites*, 23(4):261 – 265, 1992. ISSN 0010-4361. doi: https://doi.org/10.1016/0010-4361(92)90186-X. URL http://www.sciencedirect.com/science/article/pii/001043619290186X.

[19] J. Bonhomme, A. Argelles, J. Via, and I. Via. Numerical and experimental validation of computational models for mode i composite fracture failure. *Computational Materials Science*, 45(4):993 – 998, 2009. ISSN 0927-0256. doi: https://doi.org/10.1016/j.commatsci.2009.01.005. URL http://www.sciencedirect.com/science/article/pii/S0927025609000135.

[20] M. Charalambides, A. J. Kinloch, Y. Wang, and J. G. Williams. On the analysis of mixed-mode failure. *International Journal of Fracture*, 54(3):269–291, Apr 1992. ISSN 1573-2673. doi: 10.1007/BF00035361. URL https://doi.org/10.1007/BF00035361.

[21] Tsuchin Chu, W F. Ranson, and Michael Sutton. Applications of digital-image-correlation techniques to experimental mechanics. *Unknown*, 25:232–244, 09 1985.

[22] RS Components. Epoxy adhesive applicator gun. https://au.rs-online.com/web/p/acrylic-adhesives/9054573/.

[23] ASTM D5528. Mode i interlaminar fracture toughness of unidirectional fiber-reinforced polymer matrix composites. *International Standards*, 2014.

[24] ASTM D6671/D6671M. Standard test method for mixed mode i-mode ii interlaminar fracture toughness of unidirectional fiber reinforced polymer matrix composites. *International Standards*, 2014.

[25] F. Ducept, D. Gamby, and P. Davies. A mixed-mode failure criterion derived from tests on symmetric and asymmetric specimens. *Composites Science and Technology*, 59(4):609 – 619, 1999. ISSN 0266-3538. doi: http://dx.doi.org/10.1016/S0266-3538(98)00105-5. URL http://www.sciencedirect.com/science/article/pii/S0266353898001055.

[26] EFunda. Epfm: The j-integral. *eFunda*, 2018.

[27] P. Elisa. *Virtual Crack Closure Technique and Finite Element Method for Predicting the Delamination Growth Initiation in Composite Structures*. INTECH Open Access Publisher, 2011. ISBN 9789533074498. URL https://books.google.com.au/books?id=WCHUoAEACAAJ.

[28] Ozen Engineering. Fracture mechanics in ansys r16. http://www.ozeninc.com/new-webinar-series-fracture-mechanics-in-ansys-r16/, March 2015.

[29] B. Harris. Engineering composite materials. The Institute of Materials, 1999.

[30] Henkel. Safety data sheet loctite double bubble. http://mymsds.henkel.com/mymsds/Search.do?BUSAREA=0006&DOCTYPE=MSDS&COUN 2018.

[31] Hexcel. Glass fibre pre-preg properties. http://www.hexcel.com/Resources/DataSheets/Prepreg.

[32] RC Hibbeler and Vijay Sekar. *Mechanics of Materials*. Unknown, 10 2013. ISBN 9780133254426.

[33] Ryan J. Sager, Patrick J. Klein, Daniel Davis, Dimitris C. Lagoudas, Graham L. Warren, and Hung-Jue Sue. Interlaminar fracture toughness of woven fabric composite laminates with carbon nanotube/epoxy interleaf films. *Unknown*, 121:2394 – 2405, 08 2011.

[34] Stephen A. Jones and Rachel A. Tomlinson. Investigating mixed-mode (i/ii) fracture in epoxies using digital image correlation: Composite giic performance from resin measurements. *Engineering Fracture Mechanics*, 149(Supplement C):368 – 374, 2015. ISSN 0013-7944. doi: https://doi.org/10.1016/j.engfracmech.2015.08.041. URL http://www.sciencedirect.com/science/article/pii/S0013794415004968.

[35] MJ Laffan, ST Pinho, P Robinson, and AJ McMillan. Translaminar fracture toughness testing of composites: A review. *POLYMER TESTING*, 31:481–489, 2012. doi: 10.1016/j.polymertesting.2012.01.002. URL http://dx.doi.org/10.1016/j.polymertesting.2012.01.002.

[36] LOCTITE. Loctite hysol 3421 epoxy adhesive. http://www.loctite.co.uk/loctite-4087.htm?nodeid=8802624405505, .

[37] LOCTITE. Loctite 3421 data sheet. Technical Process Bulletin, .

[38] George Marsh. Airbus a350 xwb update. https://www.materialstoday.com/composite-applications/features/airbus-a350-xwb-update/, November 2010.

[39] V. Molln, J. Bonhomme, J. Via, and A. Argelles. Mixed mode fracture toughness: An empirical formulation for g i / g ii determination in asymmetric dcb specimens. *Engineering Structures*, 32(11):3699–3703, 2010. ISSN 0141-0296.

[40] Toshio Ogasawara, Norio Arai, Ryoichi Fukumoto, Takeshi Ogawa, Tomohiro Yokozeki, and Akinori Yoshimura. Titanium alloy foil-inserted carbon fiber/epoxy composites for cryogenic propellant tank application. *Advanced Composite Materials*, 23(2):129–149, 2014. doi: 10.1080/09243046.2013.844756. URL https://doi.org/10.1080/09243046.2013.844756.

[41] Qin Qian and De Xie. Analysis of mixed-mode dynamic crack propagation by interface element based on virtual crack closure technique. *Engineering Fracture Mechanics*, 74(5):807 – 814, 2007. ISSN 0013-7944. doi: https://doi.org/10.1016/j.engfracmech.2006.05.025. URL http://www.sciencedirect.com/science/article/pii/S0013794406002463.

[42] Ramsharan Rangarajan. Introduction to the j-integral. *Mechanical Engineering*, 2016.

[43] Johannes Reiner. A computational investigation of failure modes in hybrid titanium composite laminates, 2016.

[44] Johannes Reiner, Juan Pablo Torres, Martin Veidt, and Michael Heitzmann. Experimental and numerical analysis of drop-weight low-velocity impact tests on hybrid titanium composite laminates. *Journal of Composite Materials*, 50(26):3605–3617, 2016. doi: 10.1177/0021998315624002. URL https://doi.org/10.1177/0021998315624002.

[45] Johannes Reiner, Juan Pablo Torres, and Martin Veidt. A novel top surface analysis method for mode i interface characterisation using digital image correlation. *Engineering Fracture Mechanics*, 173:107–117, March 2017. ISSN 0013-7944.

[46] M. M. Shokrieh and A. Zeinedini. A novel method for calculation of strain energy release rate of asymmetric double cantilever laminated composite beams. *Applied Composite Materials*, 21(3):399–415, Jun 2014. ISSN 1573-4897. doi: 10.1007/s10443-013-9328-5. URL https://doi.org/10.1007/s10443-013-9328-5.

[47] Sigmaaldrich. Epoxy silane material data sheet. https://www.sigmaaldrich.com/catalog/product/aldrich/440167?lang=en&region=AU, May 2014.

[48] Tamer Sinmazelik, Egemen Avcu, Mustafa zgr Bora, and Onur oban. A review: Fibre metal laminates, background, bonding types and applied test methods. *Materials & Design*, 32(7):3671 – 3685, 2011. ISSN 0261-3069. doi: https://doi.org/10.1016/j.matdes.2011.03.011. URL http://www.sciencedirect.com/science/article/pii/S0261306911001671.

[49] Steelforce. A366 steel properties. http://www.steelforce.com.au/Article-Sheet-Steel-pg27111.html, 2018.

[50] Ashutosh Tiwari, Hirak K Patra, and Xuemei Wang. *Advanced Materials Interfaces*. Advanced Material Series. Wiley, Somerset, 2016. ISBN 1-119-24275-4.

[51] Unknown. Steel identification. https://www.alacero.org/en/page/el-acero/what-is-steel, .

[52] Unknown. Steel industry conference. https://www.worldsteel.org, .

[53] Unknown. Steel market development q2 2017. https://www.oecd.org/industry/ind/steel-market-developments-2017Q2.pdf, .

[54] Unknown. Gfrp market trend. https://www.marketresearchfuture.com/reports/glass-fiber-reinforced-plastic-gfrp-market-5004, 2016.

[55] Unknown. The history of gfrp. http://www.mateenbar.com/history-of-frp/, 2016.

[56] Cees van Hengel and Peter Kortbeek. Arall and glare fml's: Three decades of bridging the gap between theory and operational practice. In M. J. Bos, editor, *ICAF 2009, Bridging the Gap between Theory and Operational Practice*, pages 601–615, Dordrecht, 2009. Springer Netherlands. ISBN 978-90-481-2746-7.

[57] C. A. J. R. Vermeeren. An historic overview of the development of fibre metal laminates. *Applied Composite Materials*, 10(4):189–205, Jul 2003. ISSN 1573-4897. doi: 10.1023/A:1025533701806. URL `https://doi.org/10.1023/A:1025533701806`.

[58] Ad Vlot. *Glare: history of the development of a new aircraft material*. Unknown, 01 2001. ISBN 978-1-4020-0124-6.

[59] L Vogelesang and J. Gunnink. New developments in arall laminates. *Faculty of aerospace engineering Delft University of Technology*, 2003.

[60] M. Warner, C. D. Modes, and D. Corbett. Suppression of curvature in nematic elastica. *Proceedings of the Royal Society of London A: Mathematical, Physical and Engineering Sciences*, 466(2124):3561–3578, 2010. ISSN 1364-5021. doi: 10.1098/rspa.2010.0139. URL `http://rspa.royalsocietypublishing.org/content/466/2124/3561`.

[61] J. G. Williams. On the calculation of energy release rates for cracked laminates. *International Journal of Fracture*, 36(2):101–119, Feb 1988. ISSN 1573-2673. doi: 10.1007/BF00017790. URL `https://doi.org/10.1007/BF00017790`.

[62] Karen Wood. Wind turbine blades: Glass vs. carbon fiber. https://www.compositesworld.com/articles/wind-turbine-blades-glass-vs-carbon-fiber, May 2012.

[63] Guocai Wu and J. M. Yang. The mechanical behavior of glare laminates for aircraft structures. *JOM*, 57(1):72–79, Jan 2005. ISSN 1543-1851. doi: 10.1007/s11837-005-0067-4. URL `https://doi.org/10.1007/s11837-005-0067-4`.

[64] S. Yoneyama, Y. Morimoto, and M. Takashi. Automatic evaluation of mixed-mode stress intensity factors utilizing digital image correlation. *Strain*, 42(1):21–29, 2006. ISSN 1475-1305. doi: 10.1111/j.1475-1305.2006.00246.x. URL `http://dx.doi.org/10.1111/j.1475-1305.2006.00246.x`.

Appendix A

A.1 Resource Management

The following pages provide clarity in the Tasks assigned, who is responsible, the projects overall timeline and the required programs/tools in order for the project to be completed.

Table A.1: Human Resource Management

	Requirements			
Task	Person(s) Responsible	Hardware	Software	Documents
1.0	Shane/Martin	Computer	MS Suite/Blackboard	Thesis Workbook/Thesis Proposal
1.1	Shane/Martin	Computer/Printer	Latex/JabRef/Excel	Thesis Workbook/Project Proposal
1.2	Shane/Martin	Computer/Printer	Latex/JabRef/Excel	Thesis Workbook/Project Proposal
1.3	Shane/Martin	Computer/Printer	Latex/JabRef/Excel	Thesis Workbook/Project Proposal
1.4	Shane/Martin	Computer/Printer	Latex/JabRef/Excel	Thesis Workbook/Project Proposal
2.0	Shane	Computer	Latex/JabRef/Excel/ANSYS	Thesis Workbook/ASTM Standards/ANSYS
2.1	Shane	Computer	Latex/JabRef/Excel	Thesis Workbook/Fracture Textbooks
2.2	Shane	Computer	Latex/JabRef/Excel	Thesis Workbook/Various Articles
2.3	Shane	Computer/ARAMIS	Latex/JabRef/Excel	Thesis Workbook/ARAMIS
2.4	Shane	Computer/Materials	Latex/JabRef/Excel	Thesis Workbook/ASTM Standards
2.5	Shane	Computer	ANSYS APDL & Workbench/Python	Thesis Workbook/ANSYS/Python
3.0	Shane	Computer	ANSYS APDL & Workbench/Python	Thesis Workbook/ANSYS/Python
4.0	Shane	Computer	Latex/JabRef/Excel	Thesis Workbook
4.1	Shane	Computer	Latex/JabRef/Excel	Thesis Workbook
4.2	Shane	Computer	Latex/JabRef/Excel	Thesis Workbook/Risk Identification
5.0	Shane	Computer/Printer	Latex/JabRef/Excel	Thesis Workbook
6.0	Shane	Computer	ARAMIS	Thesis Workbook/ARAMIS
6.1	Shane	Computer	ANSYS APDL & Workbench/Python	Thesis Workbook/ANSYS/Python
7.0	Shane	Computer	ARAMIS	Thesis Workbook
7.1	Shane	Computer	ANSYS APDL & Workbench/Python	Thesis Workbook/ARAMIS
8.0	Shane	Computer	Latex/JabRef/Excel	Thesis Workbook/ANSYS/Python
9.0	Shane	Computer	Latex/JabRef/Excel	Thesis Workbook

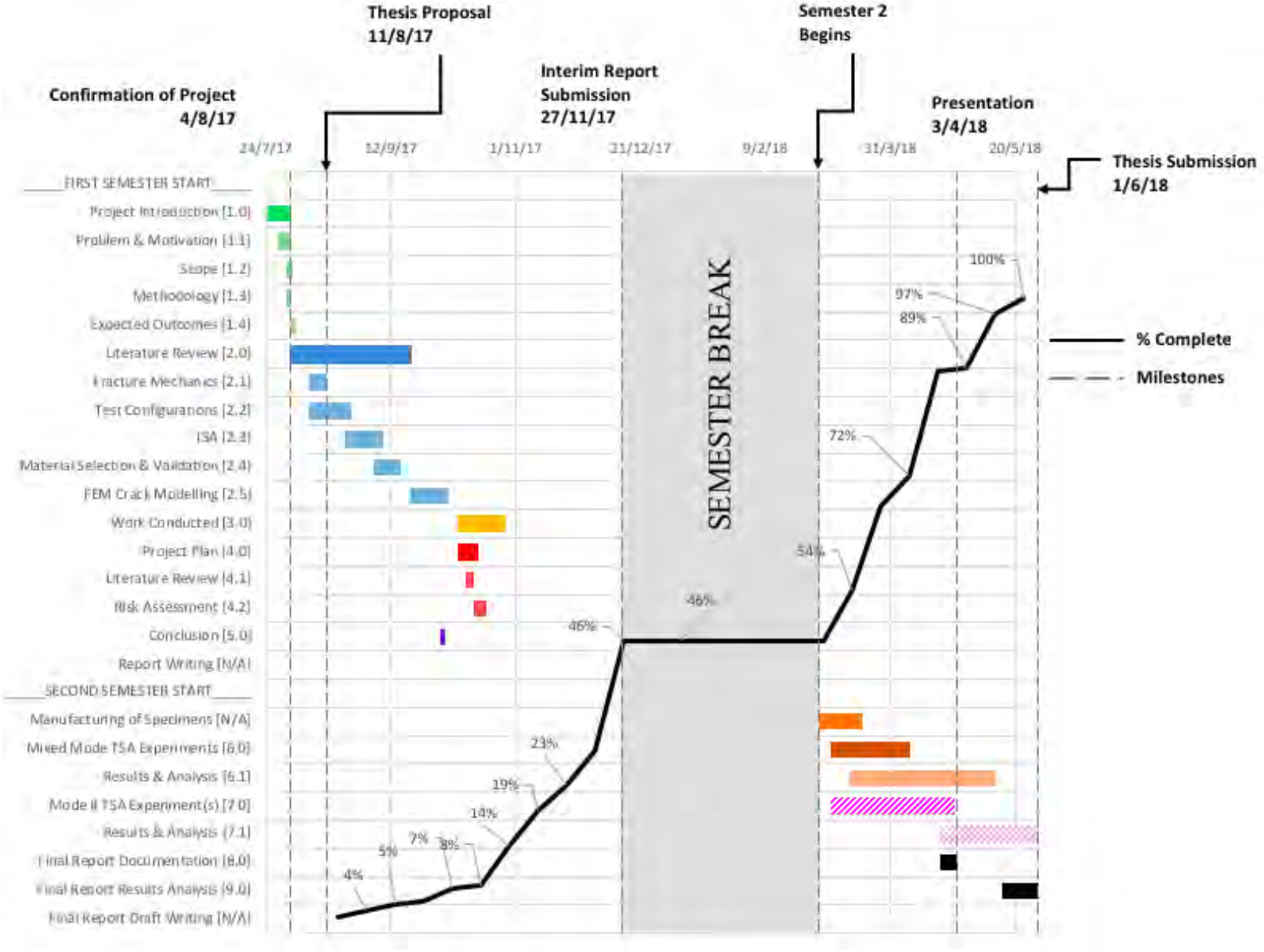

Figure A.1: Gantt Chart

A.2 Risk Assessment

Table A.2: Risk Assessment Nomenclature

Grade	Possible Action
A	Mitigation actions, to reduce the likelihood and seriousness, to be identified and implemented as soon as the project commences as a priority.
B	Mitigation actions, to reduce the likelihood and seriousness, to be identified and appropriate actions implemented during project execution.
C	Mitigation actions, to reduce the likelihood and seriousness, to be identified and costed for possible action if funds permit.
D	To be noted; no action is needed unless grading increases over time.
N	To be noted; no action is needed unless grading increases over time.

Column Index	Description with nomenclature
L - Likelihood of occurring	'L' - Low, 'M' - Medium, 'H' - High
S - Severity	As above

Table A.3: Risk Assessment

Ref #	Description	Impact on Project	L	S	G	Mitigation Actions	Person(s) Responsible
R1	Materials unable to be manufactured	Restricted in material testing and results	M	H	B	Confirmation of results at end of Sem 1	Shane/Martin
R2	Materials contain flaws/defects	Deviation of expected results	H	M	C	High material selection grades	Shane/Martin
R3	TSA Software is corrupt	No results for analysis	M	H	A	Confirmation of results at end of Sem 1	Shane/Martin/Juan
R4	TSA unable to predict fracture properties	Error in results	M	M	N	Not possible	Shane
R5	FEM results are incorrect	No basis for results from TSA	M	M	B	Seek help immediately	Shane
R6	Material particle projection during testing	Personal injury	M	M	B	PPE equipment/Online inductions	Shane
R7	Material specimens are lost	Restricted in material testing and results	L	H	B	Keep in composite labs in allocated cupboards	Shane
R8	Material specimens are dropped	Create stress concentrations/flaws	M	H	D	Avoid un-necessary relocation	Shane
R9	Material specimens contain sharp edges	Personal injury	M	L	C	PPE equipment/Online inductions	Shane
R10	Test procedure is obselete in providing results	Error in fracture properties	M	H	B	Confirmation of test selection at end of Sem 1	Shane/Martin
R11	Time management issues	Unable to allocate enough time to tasks	H	H	A	Gantt chart	Shane
R12	Medical illness causing delays	Unable to work on project	L	H	B	Not possible	Shane

Appendix B

B.1 Raw Data

Test Report

Graph 2

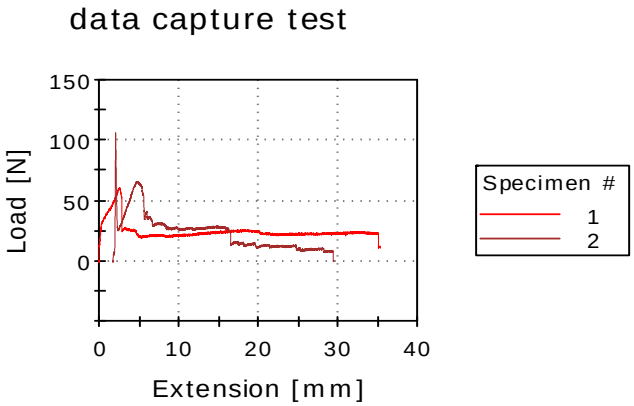

Results

	Specimen label	Diameter [mm]
1	#4	
2	#4	

Method description
Loading Rate 2.5 mm/min slow loading rate.

Rate 1	2.50000 mm/min
Method description	Loading Rate 2.5 mm/min slow loading rate.
Last test time	11:12:31 AM

Mode1_Sample_6(1)&Sample_8(2)

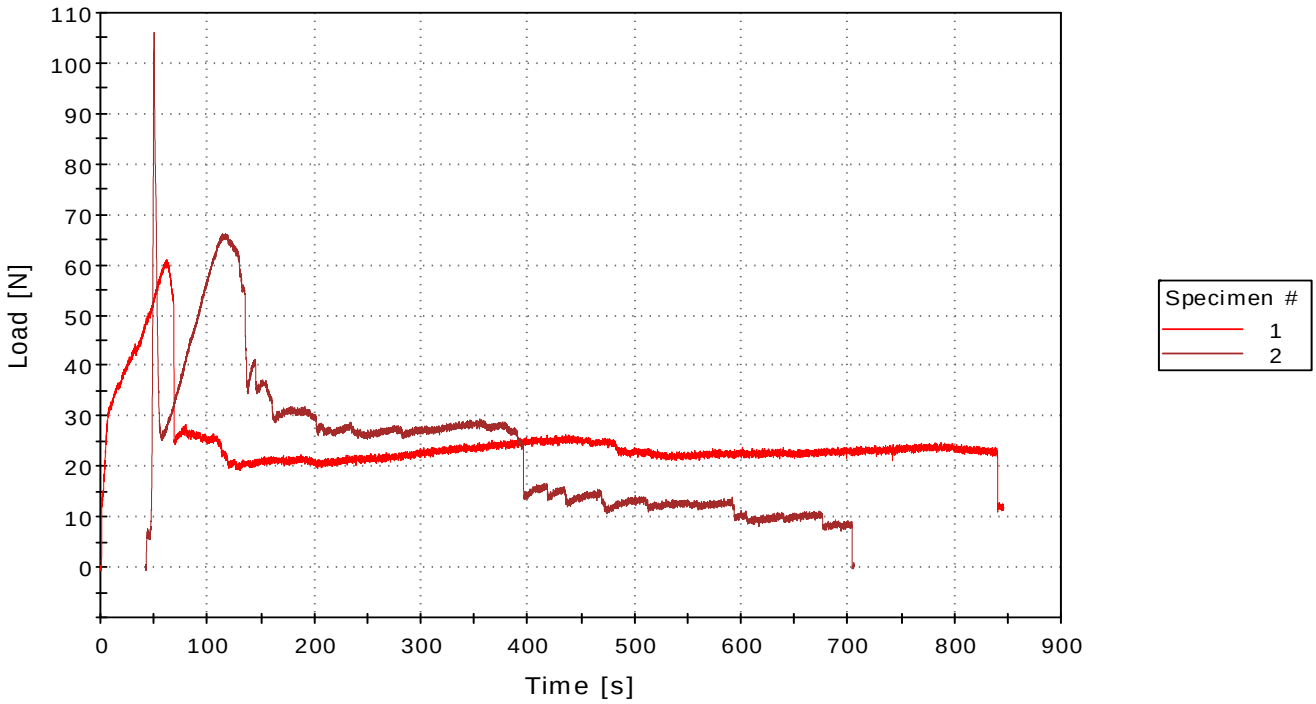

Test Report

Graph 2

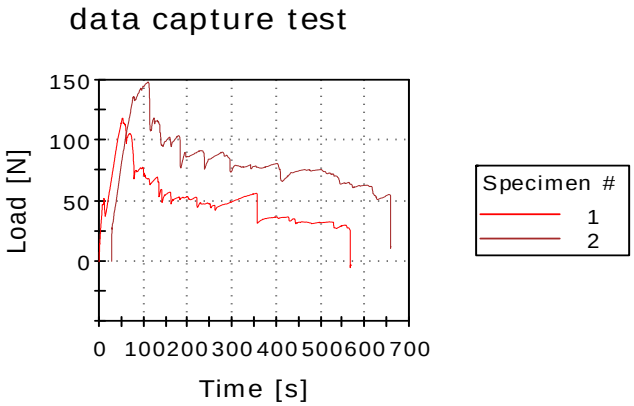

Results

	Specimen label	Diameter [mm]
1	#4	
2	#4	

Method description
Loading Rate 2.5 mm/min slow loading rate.

Rate 1	2.50000 mm/min
Method description	Loading Rate 2.5 mm/min slow loading rate.
Last test time	10:42:39 AM

Specimen 1 (#11) and Specimen 2 (#7)